



저작자표시-비영리-변경금지 2.0 대한민국

이용자는 아래의 조건을 따르는 경우에 한하여 자유롭게

- 이 저작물을 복제, 배포, 전송, 전시, 공연 및 방송할 수 있습니다.

다음과 같은 조건을 따라야 합니다:



저작자표시. 귀하는 원저작자를 표시하여야 합니다.



비영리. 귀하는 이 저작물을 영리 목적으로 이용할 수 없습니다.



변경금지. 귀하는 이 저작물을 개작, 변형 또는 가공할 수 없습니다.

- 귀하는, 이 저작물의 재이용이나 배포의 경우, 이 저작물에 적용된 이용허락조건을 명확하게 나타내어야 합니다.
- 저작권자로부터 별도의 허가를 받으면 이러한 조건들은 적용되지 않습니다.

저작권법에 따른 이용자의 권리는 위의 내용에 의하여 영향을 받지 않습니다.

이것은 [이용허락규약\(Legal Code\)](#)을 이해하기 쉽게 요약한 것입니다.

[Disclaimer](#)

Ph.D. DISSERTATION

**First-principles study on the oxygen vacancy
in semiconducting oxides**

By

Sang Ho Jeon

August 2012

**Department of Materials Science and Engineering
College of Engineering
Seoul National University**

**First-principles study on the oxygen vacancy
in semiconducting oxides**

Advisor : Prof. Seungwu Han

By

Sang Ho Jeon

**A thesis submitted to the Graduate Faculty of Seoul National
University in partial fulfillment of the requirements
for the Degree of Doctor of Philosophy
Department of Materials Science and Engineering**

August 2012

Approved

By

Chairman of Advisory Committee : Kisuk Kang

Vice-chairman of Advisory Committee : Seungwu Han

Advisory Committee : Cheol Seong Hwang

Advisory Committee : Kyeongjae Cho

Advisory Committee : Youngmi Cho

Abstract

Semiconducting oxides has been widely attractive due to its potential for alternative materials to silicon which has revealed the limitation in performance of devices consisted of it as the size of devices is decreased. Furthermore, since the enormous probability of oxides to apply to various devices due to variety properties from many compounds, semiconducting oxides will be the most promising technologies for leading the next generation of semiconductor-devices such as TFT and display panel. Interestingly, the material properties of oxides, especially electrical properties, critically depend on the presence of lattice imperfections such as the grain boundary and point defects. In particular, the oxygen vacancy (V_O), which constitutes a most fundamental point defect in oxides, plays crucial roles in determining the performance of various electronic devices that include the oxide materials. For instance, for the operation of resistance random access memory (ReRAM) with resistance switching phenomenon under the external field, it is widely accepted that the electromigration of the charged V_O is crucial for the formation and rupture of the local conducting path in insulating oxides. For transparent conducting oxides (TCOs) with wide band-gap, likewise, the n-type conductivity even in undoped sample is exhibited and has been revealed the strong dependence on oxygen partial pressure, indicating that V_O may play an important role in the conductivity of TCOs. Since the importance of the V_O in the material properties of oxides has been revealed, it is strongly required that the roles of V_O in oxides are sufficiently understood. However, because the nature of V_O be defined in atomic level, the study on the role of V_O needs to be performed in point of atomic scale view. Unfortunately, it does not allow us to identify the nature of V_O due to the limitation of experimental research such as the

resolution and the difficulty of direct measurement.

In this thesis, we carried out First-principles study on the V_O in oxides to approach to the full-understand about the role of V_O in oxides with respect to the three kind of point; diffusion, defect level and association of V_O . First with respect to the poorly understand experimental phenomena, we first investigated the migration of V_O in metal-oxides such as NiO, including the effect of grain boundary in poly-crystal. We found that the lattice imperfection such as the grain boundary could be the favorite path for V_O due to the lower migration barrier than bulk. Further, we also estimated the electromigration of V_O in various metal-oxides under the external electric field. We found that the lowered migration barrier though the migration path of V_O by external field can be negligible, and that the faster migration of V_O under electric field can be explained by Joule-heating effect to increase the local temperature around V_O site, giving rise to the increasing the jumping rate of atoms toward near vacant site.

Second, relating to the defect nature of V_O , we estimate the nature of V_O in TCOs such as In_2O_3 and SnO_2 in order to identify whether the V_O can contribute to the n-type conductivity of both In_2O_3 and SnO_2 or not. From the analysis of defect level and charge transition level of V_O , we found that for In_2O_3 , the nature of V_O is shallow while it is deep in SnO_2 . Even for In_2O_3 , however, the ionization energy is still large to release two electrons as free carrier at room temperature, indicating that the V_O alone in In_2O_3 cannot be origin of the intrinsic conductivity.

Key words: Density Functional Theory (DFT), Oxygen vacancy (V_O), Semiconducting oxide, TCO, ReRAM

Student number: 2010-30785

Sang Ho Jeon

Contents

Abstract.....	i
Contents.....	iii
List of figures	ix
List of Tables.....	xi
1. Introduction.....	1
1.1 Semiconducting oxides	1
1.1.1 Beyond silicon	1
1.1.2 Semiconducting oxides as alternative material for silicon.....	5
1.2 Imperfections in semiconducting oxides.....	8
1.2.1 Oxygen vacancy in oxides.....	9
1.2.2 Oxygen deficient oxides.....	10
1.3 Issues in the oxygen vacancy in oxides	11
1.3.1 The diffusion of oxygen vacancy in oxides.....	12
1.3.2 The oxygen vacancy in transparent conducting oxides	14

1.4 Objectives of the thesis.....	16
1.5 Organization of the thesis.....	18
1.6 References.....	19
2. Computation methods.....	22
2.1 Density-Functional Theory (DFT)	22
2.1.1 Hohenberg-Kohn theorems	23
2.1.2 The Kohn-Sham equations.....	25
2.1.3 Exchange and correlation in DFT.....	29
2.1.3.1 Local density approximation (LDA)	30
2.1.3.2 Generalized gradient approximation (GGA).....	31
2.1.3.3 On-site Coulomb interaction correction: LDA(GGA)+ U	32
2.1.3.4 Hybrid functional.....	33
2.2 General formalism of point defect calculation.....	34
2.2.1 Defect formation energies	34
2.2.2 Defect-defect interaction in finite cell-size	35
2.2.3 Defect charge transition energies	36

2.2.4 Band-gap correction.....	37
2.3 Diffusion of defect.....	38
2.3.1 Nudged elastic band (NEB) method.....	38
2.3.2 Harmonic transition state theory (HTST)	42
2.4 References	44
3. The migration of the V_O in metal oxides.....	45
3.1 The migration of V_O a grain boundary	46
3.1.1 Introduction.....	46
3.1.2 Computational setup.....	48
3.1.3 Results and discussion.....	51
3.1.3.1 Electronic properties of grain boundary in NiO	51
3.1.3.2 Defects formation at grain boundary	54
3.1.3.3 Density of states of point defects	58
3.1.3.3 The migration of the V_O at grain boundary	59
3.1.4 Summary.....	62
3.2 The electromigration of the charged V_O.....	63

3.2.1 Introduction.....	63
3.2.2 Computational setup.....	67
3.2.3 Results and discussion.....	68
3.2.3.1 Model slabs under the external field.....	68
3.2.3.2 Oxygen vacancies.....	72
3.2.3.3 Kinetic Monte Carlo simulations	78
3.2.4 Summary.....	81
3.3 References.....	83
4. The nature of V_O in metal oxides	87
4.1 The nature of V_O in In_2O_3	88
4.1.1 Introduction.....	88
4.1.2 Computational setup.....	90
4.1.3 Results and discussion.....	94
4.1.3.1 Relaxation pattern of atoms around V_O site	94
4.1.3.2 Formation energy of charged V_O	97
4.1.3.3 Defect charge transition level.....	100

4.1.3.4 Defect energy level in band gap	100
4.1.3.5 The effective radius of defect state.....	104
4.1.3.6 The association of V_O 's.....	105
4.1.3.7 The effect of pre-existing V_O 's.....	108
4.1.3.8 The effect of carrier density.....	108
4.1.4 Summary.....	109
4.2 The nature of V_O in SnO_2.....	110
4.2.1 Introduction.....	110
4.2.2 Computational setup.....	111
4.2.3 Results and discussion.....	115
4.2.3.1 Relaxation pattern of atoms around V_O site	115
4.2.3.2 Band structures of SnO_2 containing V_O	119
4.2.3.3 Thermal ionization energy	121
4.2.3.4 Optical ionization energy	121
4.2.4 Summary.....	122
4.3 References.....	123

5. Conclusion	126
5.1 References	129

List of figures

Figure 1.1.1 MOSFET cross section	4
Figure 1.3.1 I-V characteristics of a combined Pt/NiO/Pt/ <i>p</i> -NiO _x / <i>n</i> - NiO _x /Pt structure, namely, 1D/1R structure.....	13
Figure 1.3.2 Dependence of carrier concentration on oxygen partial pressure for a-IGZO and a-IZO.....	15
Figure 2.1 Schematic illustration of a two-dimensional energy surface with two local minima separated by a transition state	41
Figure 3.1.1. Model structure of GB in NiO	50
Figure 3.1.2. Density of states of GB.....	53
Figure 3.1.3. Formation energies of V_{Ni} and V_O	56
Figure 3.1.4 The density of states of V_{Ni} and V_O	57
Figure 3.1.5 The activation energy of migration of V_O at GB	61
Figure 3.2.1 The geometry of model slabs.....	66
Figure 3.2.2 The macroscopically averaged potential differences and the local permittivity	71
Figure 3.2.3 The energy change with respect to vacancy positions in different layers.....	74
Figure 3.2.4 The results from nudged-elastic band methods for the charged vacancy migrating.	76
Figure 3.2.5 The kinetic Monte Carlo simulations	80
Figure 4.1.1 Model structure of In ₂ O ₃	92
Figure 4.1.2 Displacement of relaxed atoms around V_O site	96

Figure 4.1.3 Formation energy of V_O in each charged state as a function of L^{-1} and V^{-1}	99
Figure 4.1.4 The transition level of V_O	102
Figure 4.1.5 (a) Energy difference between CBM and V_O defect level at the Γ point as a function of V_O density. (b) The y-z axis averaged charge distribution of V_O defect level at the Γ point	103
Figure 4.1.6 The association of V_O 's	107
Figure 4.2.1 Model structure of SnO_2	113
Figure 4.2.2 Relaxation pattern and partial charge density of V_O^0 and V_O^{2+}	117
Figure 4.2.3 Band structure of V_O	118
Figure 4.2.4 Formation enthalpy of V_O in SnO_2	120

List of Tables

Table 1.1.2 Comparison of a-Si:H and Oxide TFT.	7
Table 3.2.1 The dielectric constant of each metal-oxides.....	75
Table 4.1.1 Cell dimension and V_O density corresponding to each supercell with various numbers of atoms.....	93
Table 4.2.1 Structural parameters of SnO ₂	114

CHAPTER 1

INTRODUCTION

This chapter presents a introduction of the semiconducting oxides and of its native point defect, the oxygen vacancy. Furthermore, the crucial roles of the oxygen vacancy in the material properties and the current issues on it are summarized. Finally, the objectives of the study that will present in this thesis are briefly introduced.

1.1. Semiconducting oxides

1.1.1 Beyond silicon

Silicon-based electronics have been an attractive material to the industry for several decades, driving technology breakthroughs that affect virtually all aspects of everyday life. As all devices have become smaller, faster, more efficient, more powerful, and cheaper, the size of transistors, the building blocks of electronics, is approaching the limits of what can be done on a large-scale industrial basis. For instance, present silicon-based metal-oxide-semiconductor field effect transistor (MOSFET) (Fig. 1.1.1) technology faces with biggest problem. It has already entered the nano-scale regime and faced significant challenges arising from the need to introduce new materials and novel device structures. It is the impending replacement of the SiO_2 , the native oxide of Si, by gate insulator with the higher dielectric constant (k) ionic oxide [1~2]. The main driver for a change in materials associated with the transistor gate stack is the thickness of the gate dielectric. In order to avoid leakage currents through the gate oxide (shown in Fig. 1.1.1), alternative dielectric materials with higher dielectric constant are strongly required. [3] Furthermore, in the course of dynamic random access memory (DRAM) evolution, bit densities have increased from 16 K to 1 M bit per chip. The necessary decrease in storage capacitor size corresponding to this density-increase has been achieved primarily by decreasing the thickness of the SiO_2 storage insulator, even though capacitance enhancements have also been achieved by incorporating higher dielectric constant insulators and increasing the doping levels in the silicon. [3] Although these approaches to the high density will be pursued until physical limitations are encountered, the limitation in storage density of silicon-based capacitor has been predicted. In addition, further performance like non-volatility cannot expect in conventional devices. Therefore, new design using an alternative material for silicon has been strongly demanded for next generation devices. It seems that a replacement for silicon with the alternative materials

cannot be avoided any longer.

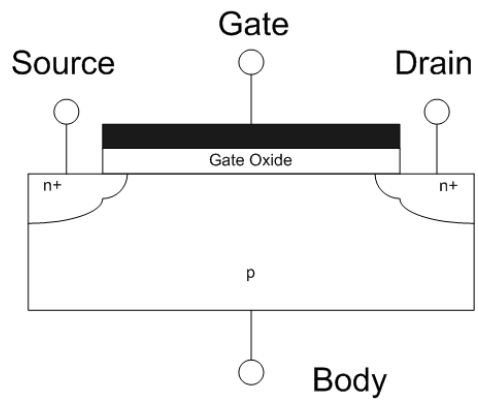


Figure 1.1.1 MOSFET cross section.

1.1.2 Semiconducting oxides as an alternative material for silicon

Beyond silicon, semiconducting oxides have been intention in many industry fields due to its potential to substitute the silicon within the traditional devices. Moreover, the advantage of oxides is, of course, based on the fact that many elements in the periodic table can form compounds with oxygen. Its enormous potential related to its varieties of compound has been attractive and widely used in various devices. These multi-component oxides have exploited the new field known as the science of strongly correlated-electron materials. For example, oxide semiconductors, especially the amorphous ones, are a promising class of thin-film transistor (TFT) (Fig. 1.1.1) materials that have made an impressive progress not only in conventional applications such as display application in a relatively short time [2] but in opening doors to completely new and disruptive areas like paper electronics [4]. a-Si has been most widely investigated material for flexible electronics and has been demonstrated to be useful in developing flexible solar cells and TFTs [5~6]. However, device performances and applications are limited by the properties inherent to this material. (Table 1.1.1) For instance, the field-effect mobilities (μ_{eff}) of a-Si TFTs are only $< 0.5 \text{ cm}^2 \cdot \text{V}^{-1} \cdot \text{s}^{-1}$. These values are not enough for high-resolution carrier injection devices such as organic electroluminescent (OEL) displays. Furthermore, amorphous materials that can be deposited at low temperatures have strongly been demanded for large-scale displays. Recently, it is well-known that amorphous oxide semiconductors (AOSs) can be deposited at room temperature and show thermal stability, and that those have much more suitable properties such as high mobility of carriers for developing flexible TFTs

than conventional amorphous silicon-based semiconductors. [7] In practice, AOS-based TFTs fabricated on polyethylene terephthalate (PET) sheets at room temperature (RT) exhibited field-effect mobilities of up to $40 \text{ cm}^2 \cdot \text{V}^{-1} \cdot \text{s}^{-1}$, which are almost two order of magnitude higher than those reported for a-Si and organic TFTs.

In case of memory, the current technology based on the charge storage, as like in flash memory [8], has become increasingly limited. The origin of the limitation is the cell size decreases and the total number of stored charges approaches just a few electrons. In addition, there is deep-seated issue that the transitional DRAM is the volatile memory: if the power is turned off, the stored data in memory is not maintained anymore. To overcome this problem, the oxide based nonvolatile memories have been considered as a next generation memories to alter the conventional DRAM. Although flash memory exhibits the nonvolatile properties [8], it has a relatively slow write/read speed which is not proper for DRAM which needs both fast write/read speed and the limitation of charge-storage. For that reason, resistance RAM (ReRAM) [9], phase change RAM (PRAM) [10], ferroelectric RAM (FRAM) [11] and nano floating gate memory (NFGM) [12] has been considered interesting candidates for the next-generation non-volatile memories with desired performance, and widely studied in order to put it on the production phase. Among them, ReRAM has been in the spotlight of researchers due to its great possibility of high bit-density by 3-dimensional stacking of oxides [13].

Table 1.1.2 Comparison of a-Si and Oxide TFT.

Characteristic	a-Si	Oxide TFT
Electron mobility	Poor 0.5 cm ² /Vs	Good 1-40 cm ² /Vs
Uniformity	Excellent	Good (amorphous type) Poor (crystalline type)
Stability	Poor	Poor
Scalable	Excellent, > 100"	Potential to 100"
Process temp.	Typical ~300 °C, some low temp. process can be ~150 °C	Typical ~200 °C, but some anneal at 350 °C
Cost	Low	Medium
Challenges	Poor mobility, poor stability	V _{th} unstable, manufacturing process not mature

1.2 Point defects in semiconducting oxides

It is widely accepted that the ideal crystals cannot be fabricated at any temperature, that is, crystals contain different structural imperfections or defects. In particular, if the imperfection is limited to one structural or lattice site and its immediate vicinity, the imperfection is termed as a point defect. Simple defects of this type include vacancies where constituent atoms are missing in the structure and interstitial atoms occupying the interstices between the regular sites. Both vacancies and interstitial atoms formed in pure crystals are commonly called native point defects, which play important roles in material properties. Besides, the native point defects also affect diffusion in solids. They are responsible for lattice diffusion; dislocation or short circuit diffusion takes place along the line defects, and GB and surface diffusion take place along the plane defects.

The technologically useful properties of a semiconductor often depend upon the types and concentrations of the defects it contains. For example, defects such as vacancies and interstitial atoms mediate dopant diffusion in microelectronic devices [14]. Such devices would be nearly impossible to fabricate without the diffusion of these atoms. In other applications, defects also affect the performance of photo-active devices [15] and sensor [16], the effectiveness of oxide catalysts [17], and the efficiency of devices for converting sunlight to electrical power [18]. To improve material performance, various forms of ‘defect engineering’ have been developed to control defect behavior within the solid [19], particularly for applications in microelectronics.

1.2.1 Oxygen vacancy in oxides

If a nonstoichiometric oxide is oxygen deficient, the predominating defects may be either V_O 's (oxygen deficit) or interstitial metal ions (excess metal), or both types of defects. For most metal-oxides, usually, the V_O has lower formation energy than interstitial metal ions. It indicates that it is dominant defect in metal oxides under oxygen deficient condition is V_O . As mentioned above, crystals have imperfections as like native point defects. Therefore, The V_O has been considered as a fundamental defect in metal oxides.

As well as the presence of V_O , its effective charge is also important for electronic devices and is strongly related to the materials properties with respect to the performance instability. In general, when vacancies are present when atoms on normal sites are missing, part or all of the actual charge of the missing atom also be absent from the vacant site. For instance, an oxygen atom on a normal site is removed from the crystal, the two negative actual charges, i.e., two electrons, of the oxygen ion are left in the crystal. If both of these electrons are localized at the V_O , the V_O has two negative actual charges; the charge is the same as in a perfect crystal, thus oxygen vacancy has zero effective charge. One or both of the localized or trapped electrons may be excited or ionized and transferred away from the doubly ionized, respectively. The ionized oxygen vacancies will have an effective positive charge with respect to the perfect crystal since the electrons are removed. It has long been well-known that bulk defects in

semiconductors can be electrically charged. This charge has influent on defect structure, thermal diffusion rate, trapping rates of electrons and holes, and luminescence quenching rates.

1.2.2 Oxygen deficient oxides

As usual, the oxygen deficient oxides exhibit the better material properties than the stoichiometric oxides. It indicates that the V_O in oxides plays a crucial role in material properties to affect the desired performance of devices. For example, the resistance switching in ReRAM controlled by the electric field is widely explained by the redistribution of the V_O [20] or by the formation pre of metallic phase [21] in oxygen deficient condition due to the migration of oxygen vacancies. For transparent conducting oxides (TCOs), their n-type conductivity shows the strong dependence on the oxygen partial pressure of the deposition condition, that is, the carrier concentration is decrease as the oxygen partial pressure increase. [22] It indicates that the oxygen deficient TCOs have high electron carrier and they are sufficient to use transparent electrodes. On the other hand, the oxygen deficient condition can be at a disadvantage in device performance. For AOS-based display, they exhibit the photo-induced threshold voltage shift, i.e., negative bias illuminate stability [23]. The origin of reliability problem by light illumination has been regard as the presence of the positively charged V_O at interface between metal and oxides, trapping holes. For that reason, if one want to use oxide for applications, the defect engineering to sufficiently control the V_O is strongly required

after full-understanding on the role of the V_O in oxides.

1.3 Issues in the oxygen vacancy in oxides

The technologically useful properties of a semiconducting oxides often depend upon the concentrations of the V_O it contains. The V_O in oxides has been investigated most intensively as it provides outstanding material properties. In spite of its importance, the nature of V_O has not been fully understood. In particular, the atomic scope observation has not been carried out because of the limitation of the experimental approaches. Namely, the atomic scale observations using the elaborate measurements such as transmit electron microscopy (TEM) have been tried to investigate the V_O -related material properties. It is still hard to estimate on the properties of V_O as well as its concentration in sample directly. To improve the material properties and to design the oxide based devices with the desired functions, the role of the V_O in oxide material properties needs to be fully understood.

The role of point defects such as the V_O can be divided into three parts: the diffusion, defect level in band gap and association of point defects. To understand the role of the V_O , therefore, it is strongly required to take into account these three points of view.

1.3.1 The diffusion of oxygen vacancy in oxides

First, for the diffusion of the V_O , we focused on the redistribution of the V_O by its self-diffusion in oxide, leading to the change of material properties; under external electric field, the rearrangement of V_O play a crucial role in material properties in electric devices consisted by oxide. In experiments, some phenomena are explained by the redistribution of oxygen vacancies under external field. For example, the resistance-switching phenomena of transition-metal oxides (Fig. 1.3.1) have been explained by the redistribution of V_O 's resulting in the change of local material properties or by the formation and rupture of filament path through the migration of V_O 's. [24].

However, there are no direct evidences to prove where they are distributed due to the experimental limitation not to allow to measure the local concentration of V_O . Furthermore, it is not revealed how fast the V_O can migrate through lattice site with a certain activation energy, and what the electric field affect to the activation energy, which means how degree of the energy can be lowered by the external field.

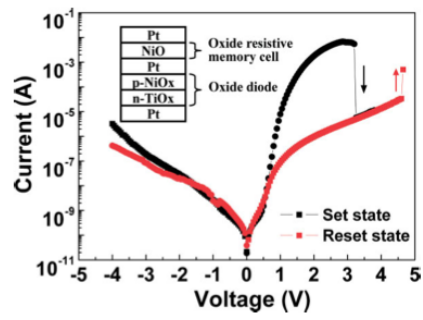


Figure 1.3.1 I-V characteristics of a combined Pt/NiO/Pt/p-NiO_x/n-TiO_x/Pt structure, namely, 1D/1R structure. [39]

1.3.2 The defect level and the association of V_O in oxides

The position of defect state in band gap is critical to define the carrier type and the contribution to conductivity. Moreover, the nature of defects can be identified from the localization or delocalization of defect states. In particular, TCOs exhibit the contrast properties such as wide band-gap and the intrinsic n -type conductivity. The reason for intrinsic conductivity has been widely explained by the presence of the V_O because of the dependence of carrier concentration on the oxygen partial pressure, as shown in Fig 1.3.2, during the sample is deposited. [25~28] However, the nature of V_O in TCOs is not fully understood due to the discrepancy between experimental and theoretical results, even between theories. For example, the computational analysis disagrees on how deep the defect level which is crucial descriptor for the nature of V_O is, reporting that it is deep-level [29~31] or shallow level [32~34].

To solve the uncertainty of the nature of V_O , we need to focus on the estimation of the defect state of isolated V_O in TCOs such as In_2O_3 and SnO_2 . Among TCOs, they are famous materials for large concentration and high mobility of electron carrier. In addition, their intrinsic n -type conductivity is not clear yet.

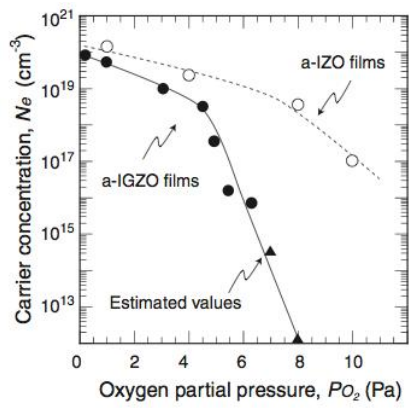


Figure 1.3.2 Dependence of carrier concentration on oxygen partial pressure for a-IGZO and a-IZO films.

1.4 Objectives of the thesis

First-principles study is a powerful tool to investigate on the nature of V_O in atomic scope instead of the experimental approach with the limitation in the scale of observation. Thus, we carried out first-principles study on the role of V_O in oxides, with respect to three points of view: the diffusion, defect nature and the association of V_O .

The thesis consists of two main parts. In the first part, in connection with the diffusion of V_O , we report the results of the migration of the V_O in GB and its electromigration under external field. In experiments, the GB is regarded as a favorite path for the V_O migration since the activation energy for migration may be lower in GB than bulk due to the lattice imperfections. It is expected that the fast migration of charged V_O , related to the fast resistance switching, can be explained the lowered activation energy in GB. In experiments, on the other hand, it was suggested that the GB may be metallic due to the presence of the V_O 's with the lower defect formation energy, that is, the segregation of the V_O brings the GB into metal-rich, leading to formation metallic path. However, the difference in the migration barrier energy between bulk and the GB in oxides has not been fully understood yet. Furthermore, there is a critical discrepancy among the different experiments whether the GB is metallic. [35]

With respect to the field effect, it also has been expected for the charged V_O to migrate easily because the activation energy be lowered by local electric field. However, the field effect in relation to the migration has not estimated yet. For that, we first carried out first-

principles study to estimate the activation energy of the V_O in the GB, comparing with that in the bulk. For this study, we have constructed the low-angle GB model of NiO with anti-ferroelectric ordering. Next, we have proposed a first-principles approach to simulate directly on the charged V_O under the external field. The V_O 's could be charged by introducing the electron-accepting dopants in the slab surface. The energy change with respect to the vacancy position could be exploited as a local "dielectric-constant meter". The kinetic Monte Carlo (KMC) simulations based on the first-principles input was carried out to explain the fast redistribution of charged vacancies.

In the second part of this thesis, we focused on the defect nature of V_O in oxides and the association between V_O 's. To reveal the uncertainty of the nature of V_O , we estimated of the defect state of isolated V_O in In_2O_3 and SnO_2 , which are famous materials for high-concentration and high-mobility of carrier among TCOs. In experiments, it is well-known that the intrinsic carrier density in TCOs has a strong dependence on the oxygen partial pressure allowing one to consider the V_O as the source of carrier. [22, 25~28] However, many theoretical reports in a debate on its nature due to the uncertainty of band gap in various functional. [36~38] Besides, the spurious interaction between point defects in finite cell due to its periodicity does not allow one to describe the V_O state well. To remedy those expected artifacts in calculation, we carefully carried out the various approaches to estimate on the isolated V_O in infinite cell size. For In_2O_3 , because of the shallow nature of the V_O , there is the cell-size dependence of the relaxation pattern and formation energy. As a result, we had to increase the cell size systemically up to 1280-atoms supercell. As well, we describe the experimental band gap using the self-interaction correction or the extrapolation scheme. Based on the results, we estimated the nature of the V_O in TCOs, in connection to the role of V_O in n -type conductivity of the

material. We elucidated both thermal and optical ionization energy to identify the nature of the V_O in In_2O_3 and SnO_2 .

1.5 Organization of the thesis

The present thesis consists of five chapters. In chapter 1, we introduce the V_O in semiconducting oxides and their issues. Chapter 2 deals with the computational methods. The basic concept and the theoretical background for defect calculations are briefly summarized. In chapter 3 and chapter 4, the results and discussions are reported in detail. In chapter 3, the results on the migration of the V_O are particularly discussed through two parts. The first part will describe the results on the migration of the V_O at grain boundary in NiO as well as the non-metallic character of grain boundary. The second part announces the electromigration of the V_O in various metal oxides under the external field. Chapter 4 describe on the nature of the V_O in In_2O_3 and SnO_2 are described. The contributions of the V_O to conductivity in each oxide are discussed. Finally, chapter 5 will summarize the results.

1.6 References

- [1] S. B. Samavedam et al., Int. Electron Devices Meet. Tech. Dig. 2002, 433 (2002)
- [2] J. F. Wager, R. Hoffman, IEEE spectrum 48, 42 (2011)
- [3] J. Robertson, Rep. Prog. Phys. 69, 327 (2006)
- [4] D. Tobjork, R. Osterbacka, Adv. Mater. 23, 1935 (2011)
- [5] Thin Film Transistors, ed. C. R. Kagan and P. Andry (Marcel Dekker, New York, 2003).
- [6] J. Singh and K. Shimakawa: Advances in Amorphous Silicon (Taylor & Francis, London, 2000).
- [7] K. Nomura, H. Ohta, A. Takagi, T. Kamiya, M. Hirano and H. Hosono: Nature 432 (2004) 432.
- [8] P. Pavan, R. Bez, P. Olivo, and E. Zanoni, Proceeding of the IEEE 85, 1248 (1997)
- [9] M.-j. Lee et al. Nano Lett. 9, 1476 (2009)
- [10] M. H. R. Lankhorst, B. W. Ketelaars, and R. A. M. Wolters, Nat. Mater. 4, 347 (2005)
- [11] J. F. Scott, C. A. Paz de Araujo, Science 246, 1400 (1989)
- [12] J. W. De Blauwe, M. L. Green, L. D. Bell, M. L. Brongersma, J. Casperson, R. C. Flagan, H. A. Atwater, Appl. Phys. Lett. 79, 433 (2001)
- [13] C.-H Wang et al. IEDM 2010
- [14] S.M. Hu, Mater. Sci. Eng. R 13, 105 (1994); M.T.L. Jung, C.T.M. Kwok, R.D. Braatz, E.G. Seebauer, J. Appl. Phys. 97, 063520 (2005); P.M. Fahey, P.B. Griffin,

- J.D. Plummer, *Rev. Mod. Phys.* 61, 289 (1989).
- [15] S. Guha, J.M. Depuydt, M.A. Haase, J. Qiu, H. Cheng, *Appl. Phys. Lett* 63, 3107 (1993).
- [16] J.W. Fergus, *J. Mater. Sci.* 38, 4259 (2003)
- [17] Y. Zhang, A. Kolmakov, S. Chretien, H. Metiu, M. Moskovits, *Nano Lett.* 4, 403 (2004)
- [18] S.R. Kurtz, A.A. Allerman, E.D. Jones, J.M. Gee, J.J. Banas, B.E. Hammons, *Appl. Phys. Lett.* 74, 729 (1999)
- [19] E.C. Jones, E. Ishida, *Mater. Sci. Eng. R* 24, 1 (1998)
- [20] M.-J. Lee, S. Han, S.H. Jeon, B. H. Park, B. S. Kang, S.-E. Ahn, K. H. Kim, C. B. Lee, C. J. Kim, I.-K. Yoo, D. H. Seo, X.-S. Li, J.-B. Park, J.-H. Lee, and Y. Park, *Nano Letters* 9, 1476 (2009)
- [21] D. Kwon, K. M. Kim, J. H. Jang, J. M. Jeon, M. H. Lee, G. H. Kim, X. Li, G. Park, B. Lee, S. Han, M. Kim, and C. S. Hwang, *Nature Nanotechnology* 5, 148 (2010)
- [22] H. Hosono, *J. Non-crys. Solids* 352, 851 (2006)
- [23] B. Ryu, H.-K. Noh, E.-A. Choi, and K. J. Chang, *Appl. Phys. Lett.* 97, 022108 (2010)
- [24] M.-J. Lee, S. Han, S. H. Jeon, B. H. Park, B. S. Kang, S.-E. Ahn, K. H. Kim, C. B. Lee, C. J. Kim, I.-K. Yoo, D. H. Seo, X.-S. Li, J.-B. Park, J.-H. Lee, and Y. Park, *Nano Lett.* 9, 1476 (2009)
- [25] H. Hosono, *Thin Solid Films* 515, 6014 (2007).
- [26] K. Nomura, H. Ohta, A. Takagi, M. Hirano, and H. Hosono, *Nature* 432, 488 (2004).
- [27] K. Nomura, H. Ohta, K. Ueda, T. Kamiya, M. Hirano, and H. Hosono, *Science* 300,

1269 (2003).

- [28] K. Nomura, A. Takagi, T. Kamiya, H. Ohta, M. Hirano, and H. Hosono, *J. J. Appl. Phys.* 45, 4303 (2006)
- [29] T. Tomita, K. Yamashita, Y. Hayafuji, and H. Adachi, *Appl. Phys. Lett.* 87, 051911 (2005)
- [30] S. Lany, and A. Zunger, *Phys. Rev. Lett.* 98, 045501 (2007)
- [31] A. Janotti, and C. G. Van de Walle, *Phys. Status Solid B* 248, 799 (2011)
- [32] P. Agostron, P. Erhart, A. Klein, and K. Albe, *J. Phys.: Condens. Matter.* 21, 455801 (2009).
- [33] P. Agoston, K. Albe, R. M. Nieminen, and M. J. Puska, *Phys. Rev. Lett.* 103, 245501 (2009).
- [34] P. Reunchan, X. Zhou, S. Limpijumnong, A. Janotti, and C. G. Van der Walle, *Current Appl. Phys.* 11, S296 (2011).
- [35] C. Park, S. H. Jeon, S. C. Chae, S. Han, B. H. Park, S. Seo, and D.-W. Kim, *Appl. Phys. Lett.* 93, 042102 (2008)
- [36] P. Agoston et. al, *Phys. Rev. Lett.* 106, 069602 (2011)
- [37] S. Lany and A. Zunger, *Phys. Rev. Lett.* 106, 069601 (2011).
- [38] P. Agoston, K. Albe, R. M. Nieminen, and M. J. Puska, *Phys. Rev. Lett.* 106, 069602 (2011).
- [39] M.-J. Lee et. al, *Adv, Mater.* 19, 73 (2007)

CHAPTER 2

Computational methods

This chapter will describe the computational methods used in this thesis. The theoretical background for first-principle study and the defect calculation methods are introduced in this chapter.

2.1 Density-Functional Theory (DFT)

The application of density functional theory (DFT) calculation is rapidly becoming a

standard tool for diverse materials modeling problem in physics, chemistry, materials science, and multiple branches of engineering. DFT is a phenomenally successful approach to finding solutions to the fundamental equation that describes the quantum behavior of atoms and molecules, the Schrodinger equation, in settings of practical value. The concept of DFT is that the properties of a system of interacting particles can be expressed by a functional of the ground state density. The basic concept of DFT comes from the method of Thomas [1] and Fermi [2] in 1927. In Thomas-Fermi method, the electronic density is given by the fundamental variable of many-body problem. However, this original Thomas-Fermi method uses many approximations. For example, the exchange and correlation is neglected and the kinetic energy is given by the functional of density of non-interacting electrons. This original method is extended by Hohenberg-Kohn in 1964. They developed DFT by using an exact theory of many-body systems. [3] In Hohenberg-Kohn theorem, the physical properties of many-body systems can be expressed by unique functional of the ground state density. Therefore, DFT has become one of the most frequently used tools in computational physics and materials science.

2.1.1 Hohenberg-Kohn theorems

The entire field of DFT rests on two fundamental mathematical theorem proved by Hohenberg and Kohn and the derivation of a set of equations by Kohn and Sham in the mid-1960s. The theorem of Hohenberg-Kohn is to formulate DFT as an exact theory of

many-body systems. This theorem was developed from the intuitive idea that the energy can be given by the electronic density. This intuitive idea was proved by Hohenberg and Kohn. [3] In Hohenberg-Kohn theorem, DFT is based upon two theorems:

Theorem I: The ground-state energy from Schrodinger's equation is a unique functional of the electron density.

Theorem II: The electron density that minimizes the energy of the overall functional is the true electron density corresponding to the full solution of the Schrodinger equation.

Using these two theorems, the variational energy $E[\rho]$ is given by the density functional and expressed by the following equation:

$$E[\rho] = F[\rho] + \int \rho(r) V_{ext}(r) dr, \quad (2.1)$$

with

$$F[\rho] = \langle \Phi[\rho] | T + U_{ee} | \Phi[\rho] \rangle. \quad (2.2)$$

In Eq. 2.1, the first term indicates the functional of kinetic energy of electrons and the second term indicates the interaction between electrons and the external potential $V_{ext}(r)$. In Eq. 2.2, $\Phi[\rho]$ is the ground state of a potential and $\rho(r)$ is the ground state density. Therefore $E_0 = E[\rho]$ verifies $E_0 < E[\rho]$ for any $\rho \neq \rho'$ and E_0 is the ground state energy. The ground state density is obtained by using Rayleigh-Ritz's variational principle for the wave function. The variational principle is given by the following equation:

$$\delta\{E[\rho] - \mu\left(\int n(r)dr - N\right)\} = 0. \quad (2.3)$$

This leads to the generalization of the Thomas-Fermi equation:

$$\mu = \frac{\delta E[\rho]}{\delta n} = V_{ext}(r) + \frac{\delta F[\rho]}{\delta n}. \quad (2.4)$$

If we know the form of $F[\rho]$, we can obtain the solution of the many-body Schrodinger equation. As a universal functional, $F[\rho]$ does not depend on the external potential $V_{ext}(r)$ but depends on the electronic density. In Hohenberg-Kohn theorem, $F[\rho]$ is represented by

$$F[\rho] = \langle \Phi[\rho] | T + U_{ee} | \Phi[\rho] \rangle, \quad (2.5)$$

where $\Phi[\rho]$ is the ground state many-body wave function. However, the analytic form of $F[\rho]$ is unknown.

2.1.2 The Kohn-Sham equations

The Hohenberg-Kohn theorem does not provide a practical method to calculate the ground state energy from the density functional. The practical method was proposed by Kohn and Sham in 1965. The main idea of Kohn-Sham approach is to replace the difficult interacting many-body system with an easy auxiliary system. Kohn and Sham assumed that the ground state density of the original interacting system was equal to that of non-interacting system. Therefore, this leads to independent-particle equations for the non-interacting system that can be considered exactly soluble with all the difficult many-body terms incorporated into an exchange-correlation functional of the density. The ground state density and energy of the original interacting system can be calculated by

using the approximations of the exchange-correlation functional.

The basic idea of the Kohn-Sham approach is that a system with non-interacting electrons is exactly described by an antisymmetric wave function of the Slater determinant type of one-electron orbitals. In Hartree-Fock theory, the kinetic energy can be given by one-electron orbitals. The kinetic energy of non-interacting electrons is represented by

$$T = -\frac{\hbar^2}{2m} \sum_{i=1}^{\infty} f_i \langle \varphi_i | \nabla^2 | \varphi_i \rangle. \quad (2.6)$$

This kinetic energy of the non-interacting system can be exactly obtained if we know a system of non-interacting electrons that has same electronic density of the interacting system. However, this kinetic energy is different from the exact kinetic energy of the interacting system. Therefore, it is assumed that the equivalent non-interacting system whose ground state density coincides with that of the interacting system does exist.

The Hamiltonian of this system with N electrons is represented by

$$H = \sum_{i=1}^N \left[-\frac{\hbar^2}{2m} \nabla_i^2 + v(r_i) \right]. \quad (2.7)$$

This Hamiltonian has no electron-electron interactions. The eigenstates can be expressed by Slater determinants

$$\Phi(r) = \frac{1}{\sqrt{N_s!}} SD[\varphi_1(r_1)\varphi_2(r_2)\varphi_3(r_3)\cdots\varphi_{N_s}(r_{N_s})] \quad (2.8)$$

Here, the occupation numbers are 2 for $i \leq N_s$ with $N_s = N/2$, the number of doubly occupied orbitals. Therefore the density and the kinetic term are expressed by the following equations.

$$\rho(r) = 2 \sum_{i=1}^{N_s} |\varphi_i(r)|^2. \quad (2.9)$$

$$T_R[\rho] = -\frac{\hbar^2}{m} \sum_{i=1}^{N_s} \langle \varphi_i | \nabla^2 | \varphi_i \rangle. \quad (2.10)$$

The single-particle orbitals $\varphi_i(r)$ are the N_s eigenfunctions of the one-electron Hamiltonian

$$H_{KS} = -\frac{\hbar^2}{2m} \nabla^2 + v_R(r). \quad (2.11)$$

The universal density functional $F[\rho]$ can be expressed by the following from.

$$F[\rho] = T_R[\rho] + \frac{1}{2} \iint \frac{\rho(r)\rho(r')}{|r-r'|} dr dr' + E_{xc}[\rho], \quad (2.12)$$

Using Eq. 2.1 and 2.12, we can finally obtain the Kohn-Sham functional:

$$E_{KS}[\rho] = T_R[\rho] + \int \rho(r) v_{ext}(r) dr + \frac{1}{2} \iint \frac{\rho(r)\rho(r')}{|r-r'|} dr dr' + E_{xc}[\rho], \quad (2.13)$$

The Kohn-Sham energy functional is expressed by terms of the N_s orbitals that minimize the non-interacting electronic kinetic energy. The one-electron orbitals are the Kohn-Sham orbitals which are the result of a mathematical construction devised in order to simplify the problem. The Kohn-Sham orbitals satisfy the one-electron Kohn-Sham equations. However, the reference potential $v_R(r)$ is unknown. It should be possible to determine it by minimizing the Kohn-Sham functional with respect to the density. By using the variational principle and the rules of functional derivation, we can obtain the following equation:

$$\frac{\delta T_R[\rho]}{\delta \rho(r)} + v_{ext}(r) + \int \frac{\rho(r')}{|r-r'|} dr' + \frac{\delta E_{XC}[\rho]}{\delta \rho(r)} = \mu \quad (2.14)$$

Since the particles in the reference system interact with the reference potential, this Hamiltonian corresponds to the energy functional

$$E_{v_R}[\rho] = T_R[\rho] + \int \rho(r) v_R(r) dr, \quad (2.15)$$

Here, the ground state energy is the same as that of the interacting system. Using the variational principles, we can obtain the following equation.

$$\frac{\delta T_R[\rho]}{\delta \rho(r)} + v_R(r) = \mu_R, \quad (2.16)$$

In Eq. 2.16, μ_R is the chemical potential of the non-interacting system. This should coincide with that of the interacting system. The reference potential is obtained by comparing Eq. 2.14 and Eq. 2.16.

$$v_R(r) = v_{ext}(r) + \int \frac{\rho(r')}{|r-r'|} dr' + \mu_{XC}[\rho](r), \quad (2.17)$$

with

$$\mu_{XC}[\rho](r) = \frac{\delta \tilde{E}_{XC}[\rho]}{\delta \rho(r)}. \quad (2.18)$$

The reference potential $v_R(r)$ depends on the solutions of the one-electron Schrodinger equation. This equation should be solved self-consistently because the density used to construct the reference potential coincides with that obtained from the solutions of Eq. 2.8. The last term of the Eq. 2.17 is the exchange-correlation functional. For this term, well-defined approximations are needed.

2.1.3 Exchange and correlation in DFT

The beautiful results of Hohenberg, Kohn and Sham showed us that the ground state we seek can be found by minimizing the energy of an energy functional, and that this can be achieved by finding a self-consistent solution to a set of single-particle equations. There is just one critical complications in this otherwise beautiful formulation: to solve the Kohn-Sham equations we must specify the exchange-correlation function, $E_{xc}[\{\psi_i\}]$. It is very difficult to define $E_{xc}[\{\psi_i\}]$. In fact, the true form of the exchange-correlation functional whose existence is guaranteed by the Hohenberg-Kohn theorem is simply not known. Fortunately, there is one case where this functional can be derived exactly: the uniform electron gas. In this situation, the electron density is constant at all points in space; that is, $n(\mathbf{r})=\text{constant}$. This situation may appear to be of limited value in any real material since it is variations in electron density that define chemical bonds and generally make materials interesting. But the uniform electron gas provides a practical way to actually use the Kohn-Sham equation. To do this, we set the exchange-correlation potential at each position to be the known exchange-correlation potential from the uniform electron gas at the electron density observed at that position:

$$V_{xc}(\mathbf{r}) = V_{xc}^{\text{electron gas}}[n(\mathbf{r})] \quad (2.19)$$

This approximation uses only the local density to define the approximate exchange-correlation functional, so it is called the local density approximation (LDA). The LDA gives us a way to completely define the Kohn-Sham equation, but it is crucial to remember that the results from these equations do not exactly solve the true Schrodinger equation because we are not using the true exchange-correlation functional.

2.1.3.1 Local density approximation (LDA)

The LDA was proposed by Kohn and Sham. The LDA assumes that the exchange-correlation energy is the same as that of homogeneous electron gas with the same electron density. In a homogeneous electron gas, electrons have a uniform distribution of charges. Therefore the exchange-correlation energy can be given as the average of an energy density:

$$E_{XC}^{LDA} = \int \rho(r) \varepsilon_{XC}^{LDA}[\rho(r)] dr. \quad (2.20)$$

The exchange-correlation energy density is also expressed by

$$\varepsilon_{XC}^{LDA} = \frac{1}{2} \int \frac{\rho_{XC}^{LDA}(r, r')}{|r - r'|} dr', \quad \varepsilon_{XC}^{LDA} = \varepsilon_X^{LDA} + \varepsilon_C^{LDA}. \quad (2.21)$$

The exchange correlation energy is calculated by Eq. 2.20 and the exchange energy density is exactly given by Dirac's expression.

$$\varepsilon_X^D[\rho] = -\frac{3}{4} \left(\frac{3}{\pi} \right)^{1/3} \rho^{1/3} = -\frac{3}{4} \left(\frac{9}{4\pi^2} \right)^{1/3} \frac{1}{r_s} = -\frac{0.458}{r_s} a.u., \quad (2.22)$$

where $r_s = (3/4\pi\rho)^{1/3}$ is the mean inter-electronic distance expressed in atomic units. In addition, the correlation energy density is also represented by the following expression.

$$\varepsilon_C^{PZ}[\rho] = \begin{cases} A \ln r_s + B + C r_s + D r_s, & r_s \leq 1, \\ \gamma / (1 + \beta_1 \sqrt{r_s} + \beta_2 r_s), & r_s \geq 1, \end{cases} \quad (2.23)$$

The most accurate correlation energy density is based on the quantum Monte Carlo simulations of Ceperley and Alder. [4] This correlation functional has been

parameterized by Perdew and Zunger in 1981. [5] The LDA has proved useful and reasonably accurate in many problems. In addition, it is known that the LDA is successful approximation for many-body systems whose electronic density is both uniform (bulk metals) and less uniform systems (semiconductors and ionic crystals). However, there exist several limitations in LDA. The LDA usually overestimates the binding energy but underestimate the bond lengths. The self-interaction term in the Hartree term of the energy is not canceled by the LDA. In addition, the LDA neglects the corrections to the exchange-correlation term due to inhomogeneity even though the electronic density is not uniformly distributed. In other words, inhomogeneities in the electronic density are not taken into account. Therefore, in order to overcome these limitations, the exchange-correlation term is replaced by the gradient of the charge density.

2.1.3.2 Generalized gradient approximation (GGA)

The best known class of functional after the LDA uses information about the local electron density and the local gradient in the electron density; this approach defines a *generalized gradient approximation* (GGA). If the spatial variations in the electron density changes too rapidly to be described by LDA, the form of the exchange-correlation should be modified. Therefore, the functional in GGA include the density and its gradient. The exchange-correlation energy in GGA is expressed in the following form:

$$E_{XC}^{GGA}[\rho_\alpha, \rho_\beta] = \int f(\rho_\alpha, \rho_\beta, \nabla\rho_\alpha, \nabla\rho_\beta) d\vec{r} \quad (2.24)$$

There exist several exchange and correlation functional in GGA: Langreth-Mehl functional [6], BLYP functional [7], and Perdew-Burke-Ernzerhof (PBE) functional [8]. Among these functionals, PBE functional is one of the most widely used functional and PBE functional verifies many of the exact conditions for the exchange-correlation hole. Then, PBE shows the best agreement with experiments without fitting parameters. For instance, the binding energies and electronic spectra that are obtained by GGA are more improved compared to those in the LDA.

2.1.3.3 On-site Coulomb interaction correction: LDA(GGA)+ U

The current approximations to the exchange-correlation functionals, E_{xc} , have clear limitations when it comes to systems with so-called correlated electrons, e.g. some transition metal oxides or rare earth compounds. In these d or f metal systems, the electronic states are close to localization and the Coulomb repulsion between the electrons within an open shell is of a completely different nature than in the homogeneous electron gas, upon which LSDA and GGA are based. This should, in principles, be remedied in a more exact version of the DFT. However, it is not known how to write the appropriate functionals in a standard orbital independent way. In the mean time, a completely different approach has been developed, which is to add a Hubbard like on-site repulsion on top of the usual Kohn-Sham Hamiltonian,

$$E_U = U/2 \sum_{i,j} n_i n_j \quad (2.25)$$

to the ordinary DFT xc energy, while subtracting a double counting term. Here n_i is the occupation number of orbital $i = \{m_l, S\}$ in the relevant atomic shell l . This

method, known as LDA+ U , was first developed to be able to cope with so-called Mott insulators, i.e. systems where LDA and GGA incorrectly predict a metallic state. By construction, the resulting potential is orbital dependent. This now allows for localization of occupied orbitals. However, since DFT also incorporates exchange and correlation in some sense, care has to be taken in order to correct for double counting. Unfortunately, there is not a unique way to make this correction. It has been observed that the different treatments of the double counting term can lead to qualitatively different physics, especially at intermediate values of U , and so it is important to note which scheme is being used. However, in general the effect of the Hubbard U in the LDA+ U method is to drive the orbital occupations towards integers, and to favor insulating states over metallic ones. This may or may not be the correct physics in a given system.

The LDA+ U method has evolved since its first suggestion. The most general versions use a parametrized screened Hartree-Fock interaction for electrons within one atomic shell [9]. The renormalization of the bare exchange parameters is due to screening or correlations and depends strongly on the specific system. These parameters, e.g. U and J (in general there are $l+1$ independent parameters for a shell of angular momentum l), can be estimated by constrained DFT calculations, but often they are used as free parameters.

2.1.3.4 Hybrid functional

An accurate expression for the exchange functional in particular is a prerequisite for obtaining meaningful results from DFT. However, the exchange energy of a Slater determinant can be computed exactly. The straightforward and seemingly most appropriate strategy for arriving at the most accurate exchange-correlation energy seems to be to use the exact exchange energy and rely on approximate functionals only for the part missing in the Hartree-Fock picture, i.e., the electron correlation. In hybrid functional, the exchange-correlation energy is expressed by the following form.

$$E_{XC}^{hyb} = \alpha E_X^{HF} + (1 - \alpha) E_X^{DFT} + E_C^{DFT} \quad (2.26)$$

In Eq. 3.25, the parameter α is chosen to assume a specific value. In the hybrid functional, the exchange-correlation energy is given by a combination of DFT and Hartree-Fock exchange. This idea is originated from the observation that the trend from GGA or LDA is opposite to those of Hartree-Fock. Some properties such as the geometries, binding energies of molecular systems, and the band gap of semiconductors are well reproduced by this functional.

2.2 General formalism of supercell defect calculations

2.2.1 Defect formation energies

Within the supercell formalism for the representation of defects in a host lattice, the defect formation energy of a defect D in charge state q is defined as

$$E^f(q) = E_{tot}^d - E_{tot}^b + \mu_d + q(\text{VBM} + E_F) \quad (2.27)$$

where E_{tot}^d is the total energy of the defect-containing supercell and E_{tot}^b is the corresponding defect-free bulk supercell energy. μ_d is the chemical potential of defect in supercell. The electron chemical potential is referenced to the valence-band maximum (VBM) in the perfect system.

E_F is conventionally defined with respect to VBM, $E_F = VBM + \Delta E_F$, and is usually bounded between the VBM and the conduction band minimum (CBM), i.e., $E_V < E_F < E_C$, except in the case of degenerate doping, in which additional energy contributions due to electron-concentration-dependent band-filling effects have to be considered.

The growth conditions are reflected in the chemical potentials of atoms removed or added to the host crystal when the defect is formed. For example, O-poor/metal-rich conditions in metal oxide are present when the metal chemical potential equals that of elemental metal. For O-rich/metal-poor conditions, the oxygen chemical potential is defined as a half of the total energy of oxygen molecule, i.e., $\mu_O = \frac{1}{2} E_{tot}(\text{O}_2)$.

2.2.2 Defect-defect interaction in finite cell-size

The use of a plane-wave basis set in DFT has many advantages in computational cost and accuracy. However, the price is that one is restricted to periodic boundary conditions. Any defect formation energy, especially one for a defect with a nonzero charge, there fore obtains spurious interactions from the potentials of nearby periodic copies of the defect, the magnitudes of which depend strongly on the size of the supercell. To cancel

out the potential from the periodic images of the defect, finite-size error reduction method by Makov and Payne [10] has commonly used. It relates the energy of a defect in a cubic supercell of size L to that of the isolated defect ($L \rightarrow \infty$) limit via

$$E_{tot}(L) = E_{tot}(L \rightarrow \infty) - \frac{q^2 \alpha}{2\epsilon L} - \frac{2\pi q Q}{3\epsilon L^3} + O[L^{-5}] \quad , \quad (2.28)$$

where q is the monopole aperiodic charge, Q is the quadrupole moment of the aperiodic charge, ϵ is the relative dielectric constant of the medium in which the charges are embedded, and α is the Madelung constant, which is a property of the shape of the supercell only and is easily calculated using the Ewald method [11]. Since dipole-dipole terms do not necessarily cancel in noncubic systems, the higher-order Q contributions may also be important. The first-order term, which dominates for single highly localized defects where the monopole-quadrupole and dipole-dipole terms are small, contains the Madelung potential. The Madelung constant is defined such that $-q^2 \alpha / 2L$ is the potential energy per unit cell of an infinite periodic lattice of identical unit cells, each of which contains a point charge q plus a uniform neutralizing background, Jellium background. If defect charges are very well localized, so it is physically reasonable that the finite-size error should scale like $-q^2 \alpha / 2\epsilon L$, where the division by ϵ takes account of the polarizability of the solid.

2.2.3 Defect charge transition energies

The thermodynamic transition energy $\varepsilon(q/q')$ between two charge states q and q' describe the Fermi level E_F at which $E^f(q) = E^f(q')$. The thermal ionization energy of simple donors and acceptors equals the distance of $\varepsilon(+/0)$ from the CBM and that of $\varepsilon(0/-)$ from the VBM, respectively. Optical transitions between defect states in the gap and the band-edge energies can also be calculated from $E^f(q)$ (eq. xx) when the atomic positions of the initial state are kept during the optical (vertical) excitation or recombination process, according to the Franck-Condon principles. Thus, the optical absorption energy ε_o due to the excitation ($n = +1$ of an electron from the defect level into the CBM or the respective optical emission (luminescence; $n = -1$) energy due to the recombination of an electron from the CBM into the defect level is calculated as[12]

$$\varepsilon_o(q/q+n; ne) = E^f(q+n) - E^f(q), \quad (2.29)$$

when Fermi level is at CBM.

2.2.4 Band-gap correction

In the region surrounding a defect there may exist occupied orbitals referred to as “defect levels” that are localized around the defect site. These states, the energies of which lie in the band gap, can be derived either from former conduction-band states which have been lowered in energy by the presence of the defect, or from valence-band states which have been raised in energy. In the latter case, as the defect level is composed

of states that would be occupied in the perfect crystal, there is no problem. In the former case, however, with a localized defect orbital composed of unoccupied conduction-band states, the eigenvalue of the defect state will suffer from the well-known DFT band-gap problem [13], whereby energy gaps to conduction-band states are underestimated. If such defect states are occupied, the eigenvalue and degree of localization of the eigenstates may be underestimated. The resulting underestimation of the formation energy is an intrinsic problem of DFT calculations on defects. A common approach to try and make the DFT defect formation energy to try and make the DFT defect formation energies match experimental results is to apply a rigid shift to the energy eigenvalues of the occupied defect levels. In the case of strongly ionic insulators where the defects states are often so localized that it is unclear whether they are derived from the conduction or valence band. In these case, it is not obvious that the band-gap adjustment should be applied at all. Even worse, because such solids generally have large band gaps, ΔE_g itself is large.

The only approach likely to be able to fix this problem in a reliable manner would be to use a functional capable of correctly localizing the electron states and giving a correct gap. Such might be provided by a hybrid functional, although the fraction of exact exchange to be used could be regarded as an additional empirical parameter.

2.3 Diffusion of defect

2.3.1 Nudged elastic band (NEB) method

Because locating transition states is so important in defining chemical rates, many numerical methods have been developed for this task. There are two points that are important to consider when choosing which of these methods are the most useful. First, plane-wave DFT calculations readily provide first-derivative information from the energy surface, but not second derivatives. This means that so-called mode-following methods that find transition states by following low curvature directions from energy minima are not easily implemented in plane-wave calculations. These methods are often the methods of choice in localized basis set quantum chemistry calculations, where second-derivative information can be obtained. A second point to DFT typically requires considerable computational resources, so transition-state finding methods must converge to transition states in a small number of iterative steps.

The method is most widely used for finding transition states in plane-wave DFT calculation is the nudged elastic band (NEB) method [14]. This method was developed by Hannes Jónsson and co-workers as a refinement of earlier “chain-of states” methods. The aim of a chain-of-states calculation is to define the minimum energy path (MEP) between two local minima. This idea is illustrated in Fig 2.1, which is a contour diagram of a two-dimensional energy surface. In the figure, the MEP is represented by the smooth line connecting the reactant and product minima via the transition state. You can think of the locations labeled 0-7 in this figure as different sets of coordinates for the atoms in the system in which we are interested. We will refer to these locations as images. Calculating the energy at each images in the figure would require performing eight independent DFT calculations.

If you remember that the forces on the atoms in any configuration are defined by

$F = -\nabla E(r)$, where r is the set of coordinates of the atoms, then the images in Fig 2.1 can be separated into two groups. Images 0 and 7 in the figure are located at local minima, so $F=0$ for these images. For all the other images, the forces on the atoms are nonzero. A minimum energy path is defined in terms of the forces on images along the path: a path is an MEP only if the forces defined by any image along the path are oriented directly along the path. If you draw the vector defined by the forces on image 3 in Fig 2.1, You can see that the images in this figure do not define an MEP.

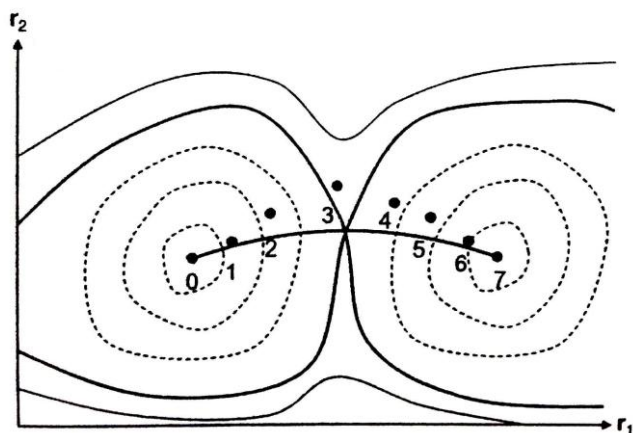


Figure 2.1 Schematic illustration of a two-dimensional energy surface with two local minima separated by a transition state. The dark curves are energy contours with energy equal to the transition-state energy. The transition state is the intersection point of the two dark curves. Dashed (solid) curves indicate contours with energies lower (higher) than the transition-state energy. The MEP is indicated with a dark line. Filled circles show the location of images used in an elastic band calculation.

2.3.2 Harmonic transition state theory (HTST)

One of the most important effects of intrinsic point defects is enhanced atomic diffusion. Vacancies and interstitials can move much more easily through the crystal than residing at ideal lattice sites in the absence of any defects. The rate of movement of defects in solids by thermal activation are given by the equation [15]

$$G = \tilde{\nu} e^{-\Delta E_a/kT} . \quad (2.30)$$

Here ΔF is the free energy needed to carry the defect from an initial equilibrium position to a saddle point, T is the absolute temperature, k is Boltzmann's constant, and $\tilde{\nu}$ is an attempt frequency associated the vibration of the defect in the direction of the saddle point. Even though only one atom jumps in the elementary process, the problem is essentially one of many bodies because the jumping atom is surrounded by other atoms with which it interacts. The approximations inherent in any rate theory are that well defined states exist for the original system (atoms near its starting point) and the transition system (atoms near the saddle point). This requires any interactions that are not a part of the phase space under consideration to be sufficiently weak. For usefulness the calculations will be simplified by two further assumptions: (a) At all stages quantum effects will be neglected. (b) At a later stage motions near the saddle point will be treated by the theory of small oscillations, i.e., the vibrations will be assumed to be nearly simple harmonic.

Consider the configuration space of the crystal. The potential energy possesses a

minimum at a point A in this space, corresponding to the atom on its original site, the vacancy on its adjoining site, and every other atom at an equilibrium position (Fig. 2.1). The another potential minimum at B, which corresponding to the atom and the vacancy interchanged in the crystal and other atoms relaxed again. By topological arguments it is seen that there must be at least one saddle point somewhere between A and B. Also, only one saddle point would be expected for the likely transitions from A to B. Label it P. Two dimensional contours of constant that these actually represent N-1 dimensional hyper-surface. There now exists a unique hyper-surface S, of dimensionality N-1, defined as follows: S passes through P and is perpendicular to the contours of constant the potential energy everywhere else. S thus separates the region around A from that around B, and any representative point reaching S with finite velocity crosses over into the region around B.

The average lifetime, τ , of representative points in region A, and the rare, Γ , of transition from A to B are related as follows:

$$\Gamma = \frac{1}{\tau} . \quad (2.31)$$

This Γ , of course, is assumed equal to the desired average jump rate already defined.

2.4 References

- [1] L. H. Thomas, Proc. Cambridge Phil. Roy. Soc. **23**, 542 (1927).
- [2] E. Fermi, Rend. Accad. Naz. Lincei **6**, 602 (1927).
- [3] P. Hohenberg and W. Kohn, Phys. Rev. **136**, 864 (1964).
- [4] D. M. Ceperley and B. J. Alder, Phys. Rev. Lett. **45**, 566 (1980).
- [5] J. P. Perdew and A. Zunger, Phys. Rev. B **23**, 5048 (1981).
- [6] D. C. Langreth and M. J. Mehl, Phys. Rev. Lett. **47**, 446 (1981).
- [7] A. D. Berke, Phys. Rev. A **38**, 3098 (1988).
- [8] J. P. Perdew, K. Berke, and M. Ernzerhof, Phys. Rev. Lett. **77**, 3865 (1996).
- [9] A. I. Liechtenstein, V.I. Anisimov and J. Zaanen, Phys. Rev. B **52**, 5467 (1995); I.V. Solovyev, A.I. Liechtenstein and K. Terakura, Phys. Rev. Lett. **80**, 5758 (1998)
- [10] G. Makov and M. C. Payne, Phys. Rev. B **51**, 4014 (1995)
- [11] P.P. Ewald, Ann, Phys. **369**, 253 (1921)
- [12] S. Lany and A. Zunger, Phys. Rev. B **72**, 035215 (2005)
- [13] L.J. Sham and M. Schluter, Phys. Rev. Lett. **51**, 1888 (1983); Phys. Rev. B **32**, 3883 (1985)
- [14] Density functional theory; a practical introduction, D. S. Sholl and J. A. Steckel, Wiley, 2009, p143
- [15] G. H. Vinyard, J. Phys. Chem. Solids **3**, 121 (1957)

CHAPTER 3

The migration of the V_O in metal oxides

This chapter will describe the migration of V_O in metal oxides to estimate the role of V_O in the material properties with respect to the diffusion phenomena in oxides, in particular, the resistance-switching in resistance random access memory (ReRAM) explained by the migration of V_O under external electric field. The NEB method is used to calculate the activation energy of V_O . Comparing the activation energy of between bulk and surface (and grain boundary), the favorite V_O migration path and site of V_O is described in this chapter. Furthermore, the migration time of V_O under external field is investigated using the harmonic transition state theory (HTST).

3.1 The migration of V_O at grain boundary

We investigated, using ab-initio plane-wave pseudo-potential method within the GGA+ U , the electronic structure and properties of the $\Sigma 5(310)[001]$ tilted GB in NiO. We found that the GB in NiO make the band gap smaller than one of single crystalline nickel oxide and that is insulating. We estimated the formation energy of defects, such as V_O , nickel vacancy (V_{Ni}), Schottky defect and nickel interstitial (Ni_i), at GB in nickel oxide. It showed that the defects can be formed easily at GB than one of bulk-like region in NiO. We also calculated the migration barrier of V_O diffusion at GB and found that it is smaller than bulk, indicating that GB can be the favor path for the ionic carriers.

3.1.1 Introduction

Resistive switching (RS) in metal oxides requires either polarity reversal or magnitude variation of the applied bias voltage. [1~10] The conducting filament formation and rupture model well describe the unipolar RS characteristics. [2~8] However, the mechanism responsible for bistable resistance states is still controversial. Polycrystalline thin films have been reported to show both bipolar and unipolar RS, [2~9] while most epitaxial thin films exhibit bipolar RS. [2,10] These observations suggest that the dominant RS mechanism may depend not only on the material but also

on its crystalline form. The material properties of polycrystalline ceramics are largely dependent on the grain boundary (GB) structures between crystalline grains. GB in rocksalt crystals such as MgO and NiO has been long-standing issues. In particular, the identification of microstructure through transmission-electron microscopes (TEM) reported that the segregation of point defects and dopants has been under extensive researches. It is explained by the enhanced diffusion of cations along GB leading to the oxidation and corrosion of the materials. As well as the investigation on MgO [11,12,13], rutile TiO₂ [14] and SrTiO₃ [15], D. M. Duffy et al. [16~18] investigated early the electronic properties of the grain boundaries in nickel oxide with rock-salt structure by experimental measurements. The theoretical study on the GB in rock-salt structures, on the other hand, has been done mostly based on the classical molecular dynamics simulation. The interactions were just modeled by Coulomb potential plus short-range repulsive parts with semiempirical potential. Unfortunately, it was found that the diffusivity is described inaccurately, enhanced by orders of magnitude. Furthermore, full-scale first-principles calculations on the electronic structure and segregation properties have not been carried out as far as we are aware. In this paper, we report density functional studies on $\Sigma 5(310)[001]$ tilt GB. [19] We examine the electronic properties such as the energy gap. Furthermore, the cation and anion vacancies are included in the model system to investigate the segregation energies to the GB. We also estimated the migration barrier of defects at GB for comparing with those in bulk to identify whether the GB can be a favorite path for ionic carriers.

3.1.2. Computational setup

For a computational package, we use Vienna ab-initio simulation package (VASP) [20]. We use projector-augmented-wave potentials [21] for describing electron-ion interaction. The valence electron configurations of $3d^84d^2$ and $2s^22p^4$ were chosen for Ni and O, respectively. The energy cutoff for plane waves expanding electronic wave functions is set to 450eV. For k-point sampling using Monkhorst-Pack scheme [22], $3 \times 2 \times 1$ meshes are used for the $\sqrt{5}(310)[001]$ tilt boundary in NiO. [19] (See below.) Further increase of k-points changes the total energy less 10^{-4} eV/atom. For all calculation, we relax internal positions until Hellmann-Feynman forces are reduced to within 0.03 eV/\AA .

NiO is known to be a typical Mott-Hubbard insulator which means that the on-site Coulomb energy affects the energy gap substantially. However, such a correlated behavior is not described properly within the density-functional calculations and one needs to go beyond the conventional local density approximations. Among various approaches, LDA+ U method is known to be computationally efficient. This method has been used to study surface and defect structures of NiO. In this work, we follow the previous recipe to determine computational parameters in LDA+ U method. To be specific, we use the spin-polarized generalized gradient approximation (SGGA) [23] + U for the exchange-correlation energy of electrons and employ a rotationally invariant approach. Two set of Coulomb (U) and exchange (J) parameters are chosen to estimate reasonably the band gap of

NiO; $U = 6.3$ eV, $J = 1.0$ eV [24].

For the model system, we choose the $\Sigma 5(310)[001]$ tilt GB in NiO which has been widely studied in experiment as well as various theoretical simulations. (See Fig. 3.1.1) To be compatible with the type-II antiferromagnetic structure, four layers of NiO are included in the unit cell along [100] direction (y -axis). In our system, there are two grains to generate identical GB. To calculate the defect properties depending on the distance from GB, one of the grains is substantially larger than the other. The distance between two grains is optimized by changing the lattice parameter along [310] direction (z -axis). There are 208 atoms in total within the unit cell indicated by a dashed box in Fig. 3.1.1. The lattice parameters along x , y and z axis are 6.59, 8.34, and 37.08 Å, respectively. As mentioned in the above, NiO is a type-II antiferromagnetic material, and we consider spin-polarization of Ni atoms. We choose spin moments of Ni atoms aligned with the same spin direction within same (111) plane and alternating between neighboring planes. This uniquely determines the spin arrangement within each grain. However, there are two choices for the relative orientation between grains. We test both spin arrangements and find that more stable is the one satisfying the super-exchange condition, i.e., two nickel atoms neighboring oxygen atom have different spin-direction each other. The energy difference between two spin orientations is 0.13 eV/supercell. This corresponds to 0.016 eV per each Ni-O bond connecting grains. (There are eight such bonds within the supercell.)

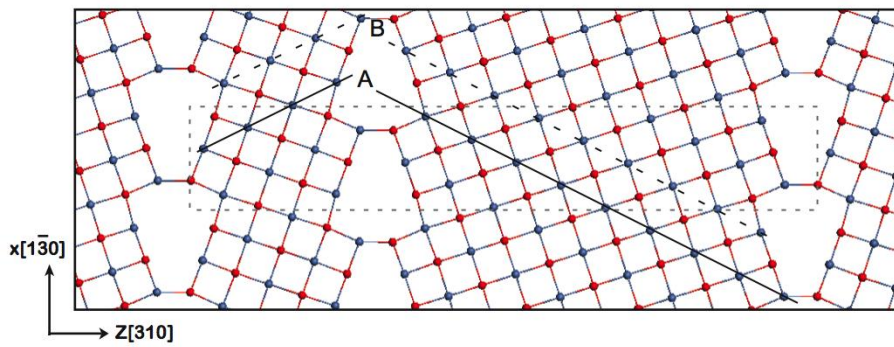


Figure 3.1.1 Model structure of GB in NiO. Unit-cell is represented by dash-line. A and B indicate the Ni atoms with same spin momentum in anti-ferroelectric NiO

3.1.3 Results and discussion

3.1.3.1 Electronic properties of grain boundary in NiO

We first calculate GB energies of our model system. It is computed to be 1.3 J/m^2 . This is in comparison with the previous results of 1.9 J/m^2 . We also calculate binding energy of GB with reference to the energies to be 1.14 J/m^2 to be compared with 1.58 J/m^2 . Although the classical potential systematically overestimates the first-principles results, the agreements are good given the fact the quantum mechanical nature is almost absent in the classical potentials. This also indicates that GB energies and binding energies are mainly Columbic nature.

We first examine the local relaxation pattern around GB. As is confirmed in Fig. 3.1.1, most of ions remain at the bulk positions except for small number of atoms right at the GB. The ions at the GB are relaxed in such a way that the bonding pattern with atoms in neighboring GB becomes more linear. The smallest separation between atoms in different grain is 1.78 \AA in comparison with a bulk value of 2.08 \AA . The reduction in the bond length can be explained by the lower coordination number than those in bulk (five vs. six).

We next discuss the electronic properties of GB in NiO. The magnetic moment of each atom is examined and it is found that the original type-II antiferromagnetic structure remains intact for the whole lattice sites. The magnetic moments of Ni atoms

are varied 1.66-1.68 μB that is very close to the bulk value of 1.67 μB . Most of oxygen atoms are spinless with very small remnant moments of $\sim 0.03 \mu\text{B}$. In Fig. 3.1.2, the total density of states (TDOS) is shown for GB. As a reference data, TDOS for crystalline NiO is also displayed. Since TDOS's for both spin directions are identical, only TDOS for one spin channel is shown. In GB-NiO, the band gap is estimated about 2.3 eV, which is smaller than bulk energy gap of 2.9 eV. As is found in Fig. 3.1.2, TDOS profile is very similar to crystalline results except for the ~ 0.6 eV tail below the conduction bottom, which accounts for the gap reduction. From the analysis on the spatial distribution of wave functions of the conduction bottom states, we find that the states is mainly Ni-eg orbitals that are loosely bound to GB. Such a reduction of energy gap at GB has been reported for other materials, for example ZnO [25].

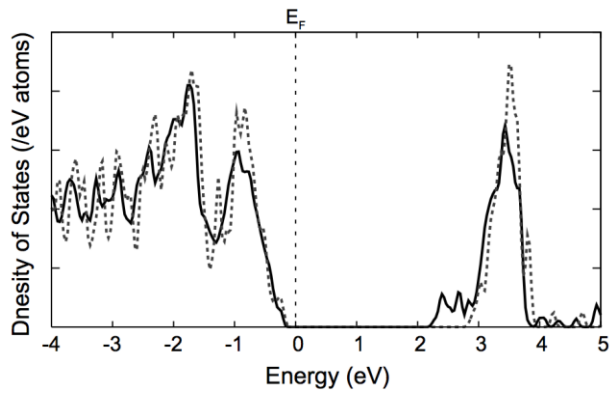


Figure 3.1.2 Density of states of GB (solid line). For comparing, DOS of bulk is also shown (dashed line)

3.1.3.2 Defects formation at grain boundary in NiO

We investigate the interaction between various defects and GB. We first look into the nickel vacancy (V_{Ni}). It is well known that the cation vacancy is dominant defect type in NiO, rendering the material a p-type semiconductor. First, we estimate the defect formation energy (E^f) of one nickel vacancy at various positions from GB.

$$\begin{aligned} E^f &= E_{\text{tot}}(V_{\text{Ni}}) + \mu_{\text{Ni}} - E_{\text{tot}}(\text{bulk}) \\ &= E_{\text{tot}}(V_{\text{Ni}}) - E_{\text{tot}}(\text{bulk}) + E_{\text{tot}}(\text{NiO}) - \mu_{\text{O}} \end{aligned} \quad (3.1)$$

where $E_{\text{tot}}(nV_{\text{Ni}})$ and $E_{\text{tot}}(\text{NiO})$ mean the total energy of the supercell including n number of V_{Ni} and the total energy per NiO formula unit for crystalline NiO, respectively. In Eq. (3.1), $\mu_{\text{Ni}} + \mu_{\text{O}} = E_{\text{tot}}(\text{NiO})$ is used. The upper bound of μ_{O} is defined by the energy of an oxygen molecule with two unpaired electrons while the lower bound is set when the chemical potential of nickel is equal to the energy of the face-centered-cubic Ni bulk. We set μ_{O} to the average of these two limits. The computed results are shown in Fig 3.1.3. (c). In our system, A, B, C, D, E and F are represented the position of nickel vacancy in the grain boundary, while the rest are bulk-like region. Our calculation shows that the formation energy of V_{Ni} is most stable at the GB region especially when it is under-coordinated (B and D). At grain boundary, especially both B and D, is negative value which is lower by 0.5 eV in bulk-like region. The difference of the formation energy between the grain boundary and bulk-like region is 0.4 ~ 0.6 eV. It is indicated that the nickel vacancy can be formed

easily and be concentrated at grain boundary than far from grain boundary. Particularly, a V_{Ni} adjacent to a oxygen atom mediating connection between two grain, C and $E-V_{Ni}$, is most unstable. We think of that superexchange interaction between two nickel-atoms mediated one oxygen atom affect the instability relative to formation energy of nickel vacancy.

Fig. 3.1.4 b) shows the DOS of defective GB-NiO with one V_{Ni} . We plot the DOS corresponding special positions. Fermi level is set to 0 eV. In the total DOS of F, presence of nickel vacancy in bulk-like region, it is showed that Fermi level is shift to top of valence band and that localized states of Ni_{eg} are appeared, which is different with the results of bulk-NiO showed that half-metallic property is appeared in presence of one nickel vacancy. When one V_{Ni} is in bulk-NiO, Fermi level shifts toward valence band and unoccupied energy band exist in majority spin-direction while minority spin are fully occupied.

The other total DOS show that GB-NiO is insulating when single nickel vacancy (or a defect) exist commonly in vicinity of grain boundary, unlike half-metallic behavior of bulk-NiO. Unoccupied states are appeared in band gap. Case of B and D, most stable position for nickel vacancy, the localized states in the vicinity of bottom of conduction band look to be a part of conduction band. It may contribute to make the band gap smaller about 0.45 eV.

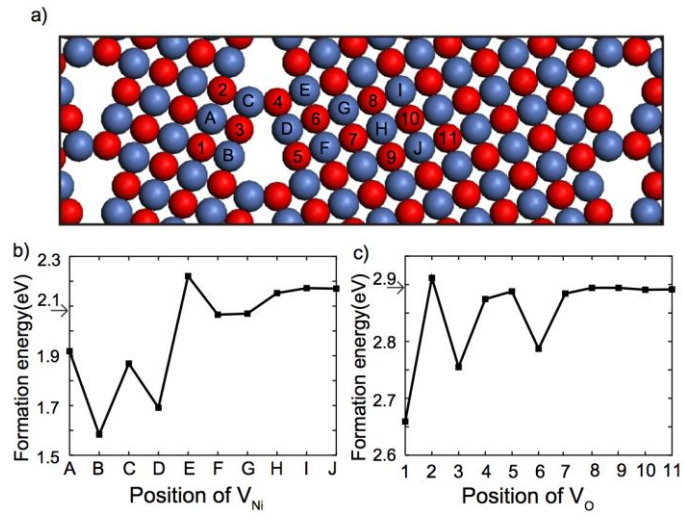


Figure 3.1.3 Formation energies of (b) V_{Ni} and (c) V_O . (a) The defect position around GB we considered are shown. The formation energy of each defect in bulk is indicated by arrows.

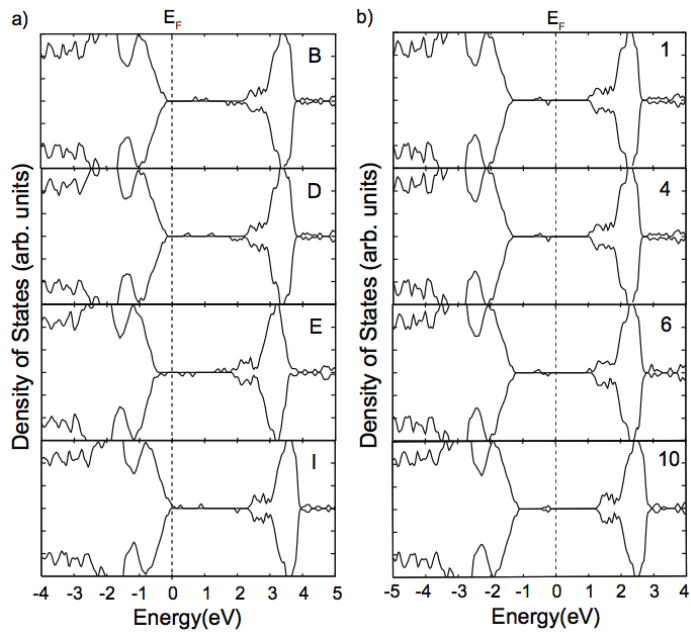


Figure 3.1.4 Density of states of V_{Ni} (left panels) and V_O (right panels) at various defect positions. The each position of defects are displayed at the upper right corner.

And anion vacancy such as V_O is also important defect in NiO such as metal oxide because metal oxide usually become deficient in growth condition of low oxygen pressures. Next, we estimate the formation energy of V_O both at grain boundary and in bulk-like region. Using cubic supercell with 64 atoms, we find that the formation energy of a V_O is 2.9 eV in bulk-NiO to compare with the results of GB-NiO. The formation energies of V_O in GB-NiO are showed in Fig. 3.1.3 c). We plot formation energy of oxygen as a function of position, and numbers mean the position of each atom in Fig. 3.1.3 a). This result showed that formation energy of V_O at grain boundary, especially at sub-surface, second layer from the interface of grain boundary, is lower than the other cases, position of 7~11, are close to the formation energy of bulk-NiO of 2.9 eV. We assumed this region as bulk-like region. In case of 2, 4 and 5- V_O , but, the formation energy is not similar with other cases at grain boundary but also they are close to that of bulk-like region. In case of 2- V_O , especially, we think of that the defect at the position is difficulty formed among all cases because super-exchange condition should be satisfied. In Fig 3.1.4. a), DOS in the presence of a V_O is showed on special position, 1, 4, 6 and 10. Among grain boundaries, the region in vicinity of surface consisted of two nickel and one oxygen is more stable than the opposite side.

3.1.3.3 Density of states of point defects

Fig. 3.1.4 a) show the DOS of GB-NiO with one V_O . We plot them of special points such as 1, 4, 6 and 10. Fermi-level is set to 0 eV. The localized states appear commonly

in all cases, and GB-NiO is insulating as like bulk-NiO. While total DOS of 10, the point in bulk-like region, show that the localized state is symmetric between spin up and down (This result is close to that of bulk-NiO showed a symmetric localized states in presence of one V_O), the others are asymmetric. The asymmetric of localized states may be produced by spin-moment of oxygen atom in vicinity of grain boundary (Fig. 3.1.1 c)).

3.1.3.3 The migration of V_O at grain boundary

Based on the our results shown that GB with point defects is not metallic, we can conclude that GB cannot be metallic path for electron carrier even if the oxygen-deficient GB is formed. Instead of metallic GB, it is possible that the GB act as the favorite path for ionic conductivity, i.e., the migration path for V_O . In general, it is described that the V_O may move easily at GB than through bulk.

To investigate the possibility of GB as a path for ionic carrier such as V_O , we calculated the activation energy of V_O at surface layer of NiO. We assumed that GB can be considered as the junction of between two surfaces with void result from lattice imperfection. Therefore, we constructed the (100) surface model system of NiO. If the initial position of oxygen atom is selected, the nearest neighbor oxygen atom is chosen as a final position of migration process. We used 5 images for the NEB calculation to find the saddle point corresponding the activation energy of the energy difference with the equilibrium ground state, initial and final state. These images including both initial and final state are described in Fig. 3.1.6. We also calculated the activation energy in bulk NiO to compare to the effect GB. We found that the amount decrease of 1 eV in

activation energy of V_O surface, resulting in the freedom normal to the surface due to the presence of vacuum. It is indicate that the V_O can be migrate at GB than bulk. Although GB is consisted of two surface with insufficient space between surfaces, the lattice imperfection at GB will allow for V_O to move though the grain surface in contrast to through bulk with perfect lattice.

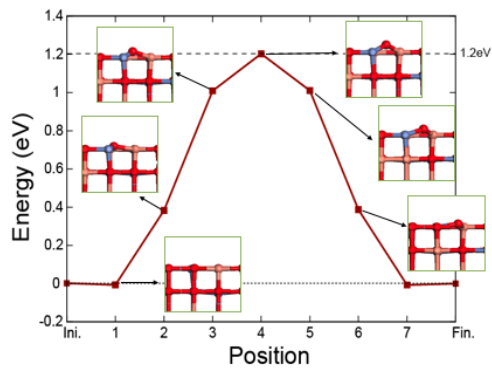


Figure 3.1.5 The activation energy of migration of V_O at GB. Inset figures represent images in the process of migration from initial to final position on the surface of grain.

3.1.4 Summary

We carried out first-principles study on the electronic properties of GB in NiO, including point defects. From our results, in contrast to the expectation to explain the current path in insulating NiO, the GB cannot be metallic even if it contains V_O which may generate free carrier to conduction band, indicating that the GB with point defects cannot be origin of the electron carrier path, i.e., filament path. However, we suggest that the ionic carrier such as V_O can be moved at GB due to the lowered activation energy. We estimated the migration barrier of V_O from NEB method and found that the activation energy is lowered by 1 eV than bulk since atoms at grain surface are forming loose bonding than bulk with lattice perfection. Finally, we can conclude that the forming and rupture of filament current path in insulating NiO can be explained by the presence of GB, in good agreements with experimental results. [26]

3.2 The electromigration of charged V_O

In an effort to simulate the charged V_O under external fields within the first-principles approach, we introduce a slab model with electron-accepting dopants in the surface. The analysis on the density of states confirms that the oxygen vacancies are positively charged. Under the external field, the total energy of the slab linearly changes with respect to the position of the charged vacancy in the field direction. From the slope of the change in the total energy, the dielectric constant around the vacancy site can be obtained, which provides a way to probe the local permittivity. The activation energy of the vacancy migration is lowered along the field direction in a manner that the charge state of the vacancy is maintained along the migration path. The kinetic Monte Carlo simulations based on the first-principles input are also carried out and it is shown that the high-temperature condition is important for the fast redistribution of charged vacancies.

3.2.1 Introduction

The material properties of metal oxides, especially electrical properties, critically depend on the presence of lattice imperfections such as the grain boundary and point defects. In particular, the V_O , which constitutes a most fundamental point defect in oxides,

plays crucial roles in determining the performance of various electronic devices that include the oxide materials. As a traditional example, the fatigue phenomena in the ferroelectric memory has been understood based on the movement of V_O driven by the electrical fields [27]. In the metal-oxide-semiconductor field effect transistor (MOSFET), high dielectric-constant materials such as HfO_2 are now replacing the traditional silicon oxides. To enhance the device performance, the high-work function metal gates are used in pair with HfO_2 in *p*-type MOSFET [28]. However, it is observed that the effective work function of the metal gate shifts to a lower value after thermal annealing [29]. It has been strongly evidenced that the creation and diffusion of the charged V_O during the annealing process play a significant role [29~32]. More recently, the importance of V_O has been receiving renewed attentions for its role in the resistance-switching random access memory (RRAM) [33~34]. To be short, the operation of RRAM is based on the soft-breakdown of oxides which can be controlled by applying the bias. The microscopic origin of RRAM is still contentious, but it is widely accepted that the electromigration of the charged V_O is crucial for the formation and rupture of the local conducting path [35~37]. Therefore, in several electronic devices, it is crucial to understand how the charged V_O drifts under the electrical bias.

Classically, the charged V_O can be regarded as a charged point particle moving with a certain activation energy, which is also partly supported by a rigorous approach [38]. However, to take into account the various local environments more realistically, it is desirable to simulate the charge V_O under the electric bias directly within the first-principles framework. As far as we are aware, there has been no attempt to apply the first-principles method to study the charged V_O in the presence of electric fields. This is in part because V_O responds to the electric field only when it is positively or negatively

charged. The charged defects are usually described by adjusting the electron numbers per unit cell. Within the periodic boundary conditions required for the plane-wave formalism, this results in the divergence of the electrostatic energy, and the uniform background charge is assumed to eliminate the Coulombic divergence. However, this makes the electric dipole of the system ill-defined since the center of the uniform charge is arbitrary. This gives rise to a problem when the external field is applied; in the presence of the uniform electric field (E_{ext}) is applied, the total energy (E_{tot}) is written as follows [29]:

$$E_{\text{tot}} = E_{\text{tot}}^{\text{KS}} - E_{\text{ext}} \cdot P, \quad (3.2)$$

where $E_{\text{tot}}^{\text{KS}}$ is the usual energy functional in the absence of the external bias and P is the polarization along the field direction. Since P is not a well-defined quantity in a system with uniform background charges, the total energy formalism is not valid any more.

In this work, the above technical problem is alleviated by introducing the charge-accepting dopants in the model system. Our results show that the charged V_{O} can be described as a charged point particle possessing the nominal charge of V_{O} to a good approximation. The present approach also provides a new way to probe the local dielectric constant. Based on the first-principles input, we also carry out the kinetic Monte Carlo simulations on the nanoscale capacitor to investigate the redistribution of V_{O} over realistic time scales.

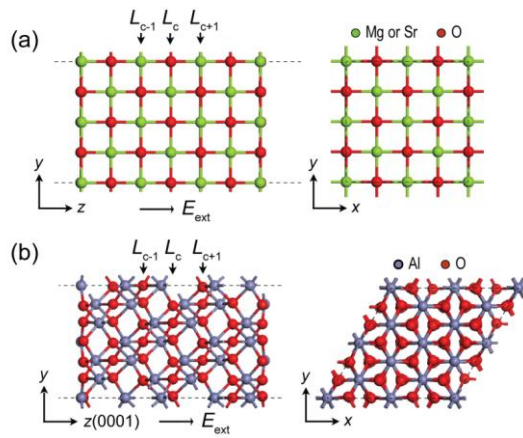


Figure 3.2.1 The geometry of model slabs. (a) MgO or SrO, and (b) α -Al₂O₃.

3.2.2 Computational setup

We carry out the density functional calculation within the local density approximation [23] for MgO, SrO, and α -Al₂O₃, three representative oxide materials. The computational package of VASP [20] is used throughout this work. We use projector-augmented-wave potentials [21] for describing electron-ion interactions. The cut-off energy for the plane-wave basis set is fixed to 500 eV. For k-point sampling, 4×4×4 and 2×2×1 meshes are used for the bulk and slab structure, respectively. Further increase of k-points changes the total energy less than 0.1 meV/atom. For all calculations, we relax atomic positions until atomic forces are reduced to within 0.03 eV/Å. For the bulk phase, it is found that the lattice parameters agree with the experiment within 2%. In order to simulate V_O under the influence of the external electric field (E_{ext}), we consider model slabs as shown in Fig. 3.2.1. The surface direction of the slab geometry (z -direction) are chosen to be (001) and (0001) for MgO (SrO) and Al₂O₃, respectively, and the external field is applied along the surface normal. The slab thickness is selected such that the dielectric constant in the middle region recovers the bulk value (see below). The V_O is introduced in one of the three layers (L_{C-1} , L_C and L_{C+1}) in the middle part of the slab (see Fig. 3.2.1). The lateral dimensions in the xy -plane are expanded to minimize the interactions between vacancies in neighboring cells. (The nearest-neighbor distances between V_O 's are 10, 12, and 13 Å for MgO, SrO, and Al₂O₃, respectively). The repeated slabs along the z -direction are separated by the vacuum of the 10 Å length, which is long enough to avoid the wave function overlap between slabs. The external field is applied

with a sawtooth potential that is compatible with periodic boundary conditions. To cancel the induced dipole fields from other slabs, the compensating is dipole layer introduced in the middle of the vacuum region [39].

As discussed in the introduction, V_O responds to the electric field only when it is positively or negatively charged but the introduction of uniform charge is not compatible with the total energy formalism. We resolve this problem by introducing the electron-accepting dopant in the slab surface. For example, if one of Mg sites in both surfaces of the MgO slab is replaced with the monovalent Li atoms, two electrons trapped in the vacancy site fall into the acceptor sites, leaving behind the doubly ionized V_O^{+2} . Similarly, Na and Be atoms are employed in SrO and Al_2O_3 slabs. From the analysis on the density of state (DOS), it is confirmed that the dopants affect the only the neighboring oxygen atoms. However, there still remains the electrostatic interaction between the neighboring charged dopants and the positively charged V_O . To eliminate the effect of this interaction from the results, we focus on the differentials of various physical quantities between with and without external biases.

3.2.3. Results and discussions

3.2.3.1 Model slabs under the external field

We first examine on the effects of the external fields on the model slab without

vacancies or dopants. The external field redistributes electrons and ions, which gives rise to the change in the electrostatic potential. It is convenient to define planar-averaged potential $\Delta V(z)$ as follows:

$$\Delta V(z) = \frac{1}{A} \int_A [V_{\text{loc}}(x, y, z; E_{\text{ext}}) - V_{\text{loc}}(x, y, z; 0)] dx dy, \quad (3.3)$$

where A is the area of the surface unit cell in the xy -plane, and $V_{\text{loc}}(x, y, z; E)$ is the sum of ionic and Hartree potentials under the external field of E . To smear out the atomic-scale oscillations, the macroscopic average is performed [40];

$$\Delta \bar{V}(z) = \frac{1}{l} \int_{z-l/2}^{z+l/2} \Delta V(z') dz' \quad (3.4)$$

where l is the length of bulk periodicity along the field direction. Fig. 3.2.2 shows $\Delta \bar{V}(z)$ for each slab when E_{ext} of 0.5 V/\AA is applied. The magnitude of the external field is confirmed by the potential slope in the vacuum space. The slope of $\Delta \bar{V}(z)$ is significantly reduced inside the slab, which essentially represents the dielectric response of the system. From the inverse ratio of the slope in the middle of the slab to E_{ext} , the local static permittivity [$\varepsilon^0(z)$] can be obtained.

$$\varepsilon^0(z) = -E_{\text{ext}} \left/ \frac{d}{dz} \Delta \bar{V}(z) \right. \quad (3.5)$$

The dashed lines in Fig. 3.2.2 indicate $\varepsilon^0(z)$. It is found that $\varepsilon^0(z)$ is enhanced near the surface region. This might be attributed to the weakened bonding between surface atoms. A similar observation was also found in Ref. [41]. The bulk dielectric constant corresponds to the value in the middle of each slab. This is summarized in Table 3.2.1. For comparison, the experimental data ($\varepsilon_{\text{exp}}^0$) and the theoretical value in the crystalline structure ($\varepsilon_{\text{bulk}}^0$) are also displayed. The theoretical values were calculated within the density functional perturbation formalism [44]. The agreements between these values

are satisfactory.

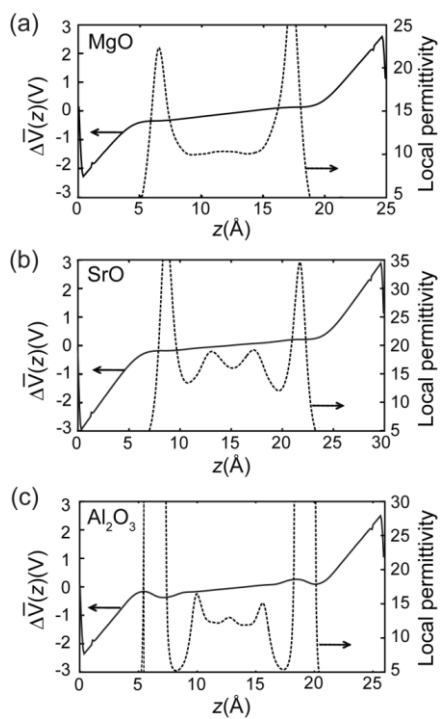


Figure 3.2.2 The macroscopically averaged potential differences (solid lines) and the local permittivity (dashed lines).

3.2.3.2 Oxygen vacancies

Next, we introduce V_O in the middle of each slab and calculate the energy difference ΔE defined as follows:

$$\Delta E = E_{\text{tot}}(0.5\text{V/\AA}) - E_{\text{tot}}(0\text{V/\AA}), \quad (3.6)$$

where $E_{\text{tot}}(E_{\text{ext}})$ is the total energy under the external field of E_{ext} .

In the absence of electron-accepting dopants, the V_O remains to be neutral, and ΔE among different layers change less than 0.05 eV. This is because the neutral vacancy does not respond to the external field. However, when the dopants are introduced in the surface layer, the V_O is doubly ionized (V_O^{+2}). This is confirmed by examining DOS, which shows that the defect levels associate with V_O lie above the Fermi level and therefore empty.

Fig. 3.2.3 (a) shows ΔE with respect to the position of V_O^{+2} in the middle layers (L_{C-1} , L_C , and L_{C+1}). As V_O^{+2} moves from L_{C-1} to L_C or from L_C to L_{C+1} , ΔE should drop by $\Delta\Delta E$ as follows [34]:

$$\Delta\Delta E = \frac{2|e|E_{\text{ext}}d}{\varepsilon^0} \quad (3.7)$$

where ε^0 is the static dielectric constant at the position of V_O^{+2} and d is the interlayer spacing. By rearranging terms, one can obtain the local permittivity at the site of the vacancy as follows;

$$\varepsilon^0 = \frac{2|e|E_{\text{ext}}d}{\Delta\Delta E} \quad (3.8)$$

The values of ε^0 obtained by Eq. (7) and $\Delta\Delta E$ from Fig. 3.2.3 are summarized in Table

3.2.1 (see $\epsilon_{\text{relaxed}}^0$). It is found that they are in good agreement with ϵ_{slab}^0 or ϵ_{bulk}^0 within ~ 1 . This suggests that the energy change as the charged vacancy move around a specific position can be used to evaluate the local permittivity at that position. For example, this method can be used in studying the variation of dielectric constant near the interface [45.46]. Compared to the pervious formulations, the present approach can be employed even when the interface is laterally irregular because the V_O is spatially localized in three dimensions.

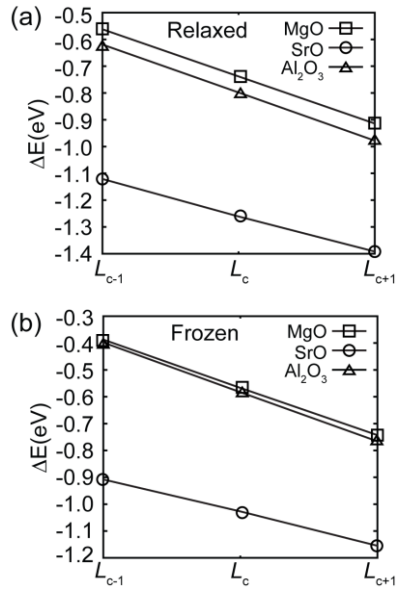


Figure 3.2.3 The energy change with respect to vacancy positions in different layers. In (a), the atomic positions are fully relaxed while the atoms in (b) are frozen to those without external fields.

Table 3.2.1. The dielectric constant of each metal-oxides.

	ϵ_{slab}^0	ϵ_{bulk}^0	ϵ_{exp}^0	$\epsilon_{\text{relaxed}}^0$	$\epsilon_{\text{fixed}}^0$
MgO	10.16	10.72	9.65 ^a	12.06	11.92
SrO	17.47	17.85	13.3 ^a	18.64	20.45
Al ₂ O ₃	12.67	11.01	9.63 ^b	12.02	11.73

^aRef. [42].

^bRef. [43]

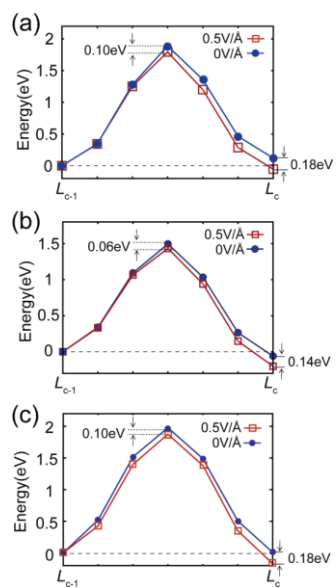


Figure 3.2.4 The results from nudged-elastic band methods for the charged vacancy migrating from L_{c-1} to L_c layers.

We also consider a case where the ionic positions are fixed to those optimized without external fields. This was motivated by the possibility of calculating the optical dielectric constant (ϵ^∞) since the lattice components of the dielectric response is excluded. The results are shown in the last column of Table 3.2.1 ($\epsilon_{\text{fixed}}^0$). Surprisingly the calculation reproduces the static dielectric constants. For comparison, ϵ^∞ for MgO, SrO, and Al₂O₃ are 3.20, 3.91, and 3.17, respectively [42,47]. We find that the relaxation energies under the external field are similar regardless of the vacancy position. However, these counterintuitive results are rather difficult to explain clearly. This result also implies that the local permittivity can be calculated without atomic relaxation under the external field, which can significantly increase the computational efficiency.

One important quantity for the dynamics of the V_O is the activation energy for the vacancy migration. The external field induces the asymmetry in the migration barrier along the field direction, which leads to the non-uniform distribution of the V_O . To investigate this in more detail, we study the migration barrier of the charged V_O under the external field by applying the nudged-elastic band (NEB) method [48]. Five equally-spaced replicas are introduced to describe the migration path between L_{C-1} and L_C layers and the results are shown in Fig. 4. The migration barriers in the absence of external fields are 1.83, 1.5, and 2.0 eV for MgO, SrO, and Al₂O₃, respectively. These values are much smaller than for the neutral vacancies since the electrons trapped in the neutral vacancy give rise to significant strain energies at the saddle point. When the external field of 0.5 V/\AA is applied, the energy barrier in the forward direction is lowered by ΔE_a as noted in each figure because the vacancy is positively charged. It can be seen that ΔE_a is very close to the half of ΔE , the energy lowered when V_O is at L_C . This is because the

transition states in these oxides are halfway between the oxygen layers. From the analysis on the atomic configuration, we find that the transition state is almost identical between biased and unbiased cases and therefore, this result indicates that the nominal charge of V_O is maintained to be $+2e$ during the migration process.

3.2.3.3 Kinetic Monte Carlo simulations

In electronic devices such as RRAM, the vacancy distribution is controlled by the bias application, and it is important to estimate the time scale to give rise to the macroscopic redistribution of vacancies. This cannot be simulated directly by first-principles methods because the system size and the time scale are far beyond the current computational capability. Instead, we investigate on this based on the kinetic Monte Carlo (KMC) method. About the model system, we assume for simplicity that oxygen sublattice forms a simple cubic structure and oxygen diffuses only through oxygen-vacancy exchange mechanism. The hopping rate (ν) between jumps is obtained from the following Boltzmann relationship:

$$\nu = \nu^* \exp\left(-\frac{E_a}{kT}\right) \quad (3.9)$$

where k and T are Boltzmann constant and temperature, respectively, and E_a is the migration barrier along the jump direction. Note that E_a is affected by the external field when the vacancy moves along the field direction. The attempt frequency (ν^*) in Eq. (3.9) is obtained within the harmonic transition-state theory (HTST) [49], which is a good

approximation for solid-state systems;

$$v^* = \frac{\left(\prod_{j=1}^{3N} \nu_j\right)_{\text{minimum}}}{\left(\prod_{j=1}^{3N-1} \nu_j\right)_{\text{saddle}}} \quad (3.10)$$

where the numerator is the product of phonon modes in the equilibrium state and the denominator is that at the saddle point excluding one imaginary value along the migration path. We obtain this value from the bulk calculation at zero external field. The phonon frequency is obtained by diagonalizing the dynamical matrix which in turn is constructed by displacing each atomic position and calculating the forces.

For the material parameters, we employ MgO. The migration barrier is then 1.83 eV from Fig. 5 and v^* from HTST is 13 THz. The lattice spacing in the oxygen sublattice is set to 2.83 Å, which is the distance between nearest-neighboring O atoms in MgO. For the KMC simulations, we adopt a simple residence-time algorithm [50]. For random number generation, a generalized feedback shift register, R250, is used [51]. For simplicity, we consider only the movement to the nearest neighbor positions, and no interaction between vacancies is assumed. The vacancy concentration is assumed to be 1% on 51×51×35 grid points (or 910 vacancies) in the simulation box.

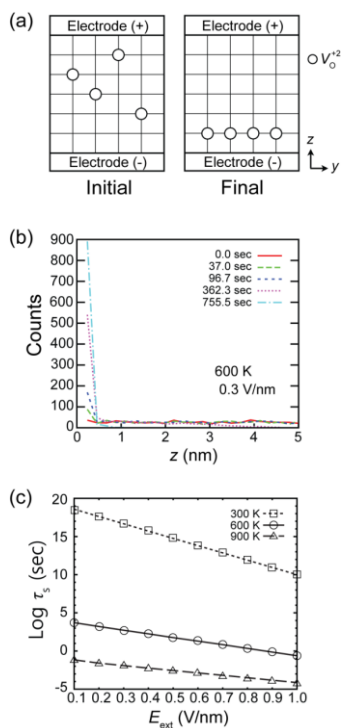


Figure 3.2.5. The kinetic Monte Carlo simulations. (a) Schematic diagram to show the initial and final geometries in kinetic Monte Carlo simulations. (b) The distribution of the VO along the field direction with respect to time. The numbers are summed over the xy -plane. (c) The set time (τ_s) as a function of the external field at various temperatures.

Fig. 3.2.5 (a) shows the schematic diagram of the simulation cell. In the initial stage, V_O 's are randomly distributed throughout the insulator. When the external bias is applied, the positively charged V_O 's are attracted to the cathode side as depicted in the right figure of Fig. 3.2.5 (a). One typical example of temporal sequence of the vacancy distribution is shown in Fig. 3.2.5 (b) assuming the electric field of 0.3 V/nm and the temperature of 600 K. To assign the characteristic response time, we define the “set time” (τ_s) as the minimum time required for accumulating 90 % of vacancies within the 0.5 nm within the cathode-insulator interface. The data on various temperatures and electric fields are shown in Fig. 3.2.5 (c). It is found that τ_s is very long at the room temperature ($T = 300$ K). Even with an electric field as high as 1 V/nm, which is close to the field emission condition, τ_s is ~ 300 years. However, if the temperature is increased to 600 K or 900 K, τ_s is greatly shortened such that the response time is in the range of the practical electronic devices. The present result confirms the experimental observation that the Joule heating is important for the resistance switching.[52]

3.2.4. Summary

In conclusion, we have proposed a first-principles approach to directly simulate the charged V_O under the external field. The oxygen vacancies could be charged by introducing the electron-accepting dopants in the slab surface. The energy charge with respect to the vacancy position could be exploited as a local “dielectric-constant meter”.

The KMC simulations based on the first-principles input was carried out and it was found that the high-temperature condition is important for the fast redistribution of charged vacancies. The present work demonstrates that the multiscale simulation of charged vacancies under the electric field is feasible by combining the first-principles approach and the KMC methods.

3.3 References

- [1] M.-J. Lee, Y. Park, D.-S. Suh, E.-H. Lee, S. Seo, D.-C. Kim, R. Jung, B.-S. Kang, S.-E. Ahn, C. B. Lee, D. H. Seo, Y.-K. Cha, I.-K. Yoo, J.-S. Kim, and B. H. Park, *Adv. Mater. (Weinheim, Ger.)* 19, 3919 (2007)
- [2] R. Waser and M. Aono, *Nat. Mater.* 6, 833 (2007)
- [3] S. C. Chae, J. S. Lee, S. Kim, S. B. Lee, S. H. Chang, C. Liu, B. Kahng, H. Shin, D.-W. Kim, C. U. Jung, S. Seo, M.-J. Lee, and T. W. Noh, *Adv. Mater. (Weinheim, Ger.)* 20, 1154 (2008)
- [4] K. M. Kim, B. J. Choi, and C. S. Hwang, *Appl. Phys. Lett.* 90, 242906 (2007)
- [5] G.-S. Park, X.-S. Li, D. C. Kim, R. Jung, M.-J. Lee, and S. Seo, *Appl. Phys. Lett.* 91, 222103 (2007)
- [6] K. Jung, H. Seo, Y. Kim, H. Im, J. P. Hong, J.-W. Park, and J.-K. Lee, *Appl. Phys. Lett.* 90, 052104 (2007)
- [7] H. Shima, F. Takano, H. Akinaga, Y. Tamai, I. H. Inoue, and H. Takagi, *Appl. Phys. Lett.* 91, 012901 (2007)
- [8] D.-W. Kim, R. Jung, B. H. Park, X.-S. Li, C. Park, S. Shin, D.-C. Kim, C. W. Lee, and S. Seo, *Jpn. J. Appl. Phys.* 47, 1635 (2008)
- [9] T. Tsunoda, Y. Fukuzumi, J. R. Jameson, Z. Wang, P. B. Griffin, and Y. Nishi, *Appl. Phys. Lett.* 90, 113501 (2007)
- [10] S. R. Lee, K. Char, D. C. Kim, R. Jung, S. Seo, X. S. Li, G.-S. Park, and I. K. Yoo, *Appl. Phys. Lett.* 91, 202115 (2007)

- [11] D. J. Harris, G. W. Watson, and, S. C. Parker, Phys. Rev. B 56, 11477 (1997).
- [12] J. H. Harding, D. J. Harris and S. C. Parker, Phys. Rev. B 60, 2740 (1999).
- [13] Y. Yan, M. F. Chisholm, G. Duscher, A. Maiti, S. J. Penny, and S. T. Pantelides, Phys. Rev. Lett. 81, 3675 (1998).
- [14] I. Dawson, P. D. Bristowe, M. H. Lee, M. C. Payne, M. D. Segall, and J. A. White, Phys. Rev. B 54, 13727 (1996).
- [15] S. Mo, W. Y. Ching, M. F. Chisholm, and G. Duscher, Phys. Rev. B 60, 2416 (1999).
- [16] D. M. Duffy, and P. W. Tasker, Philos. Mag. A 50, 143 (1984).
- [17] D. M. Duffy, and P. W. Tasker, Philos. Mag. A 47, 817 (1983).
- [18] D. M. Duffy, and P. W. Tasker, Philos. Mag. A 47, 155 (1983).
- [19] T. Karakasidls et. al, Phys. Rev. B (1997)
- [20] G. Kresse and J. Hafner, Phys. Rev. B 47, 558(R) (1993); 49, 14251 (1994).
- [21] P/ E. Blochl, Phys. Rev. B 50, 17953 (2005).
- [22] H. J. Monkhorst, and J. D. Pack, Phys. Rev. B 13. 5188 (1976).
- [23] J. P. Perdew, K. Burke, and M. Ernzerhof, Phys. Rev. Lett. 77, 3865 (1996).
- [24] A. Rohrbach, J. Hafner, and G. Kresse, Phys. Rev. B 69, 075413 (2004).
- [25] Y. Sato, and T. Tamamoto, J. Am. Ceram. Soc., 90[2] 337 (2007).
- [26] C. Park, S. H. Jeon, S. C. Chae, S. Han, B. H. Park, S. Seo, and D.-W. Kim, Appl. Phys. Lett. 93, 042102 (2008)

- [27] M. Dawber, J. F. Scott, *Integrated Ferroelectrics* 32 (2001) 259.
- [28] B. H. Lee, J. Oh, H. H. Tseng, R. Jammy, H. Huff, *Materials Today* 9 (2006) 32.
- [29] E. P. Gusev, V. Narayanan, M. M. Frank, *IBM J. Res. Dev.* 50 (2006) 387.
- [30] S. Guha, V. Narayanan, *Phys. Rev. Lett.* 98 (2007) 196101.
- [31] E. Cho, B. Lee, C. -K. Lee, S. Han, S. H. Jeon, B. H. Park, Y. -S. Kim, *Appl. Phys. Lett.* 92 (2008) 233118.
- [32] J. Robertson, O. Sharia, A. A. Demkov, *Appl. Phys. Lett.* 91 (2007) 132912.
- [33] R. Waser, M. Aono, *Nat. Mater.* 6 (2007) 833.
- [34] A. Sawa, *Materials Today*, 11 (2008) 28.
- [35] S. H. Jeon, B. H. Park, J. Lee, B. Lee, S. Han, *Appl. Phys. Lett.* 89 (2006) 042904.
- [36] K. Szot, W. Speier, G. Bihlmayer, and R. Waser, *Nature Materials* 5 (2006) 312.
- [37] D. Kwon, K. M. Kim, J. H. Jang, J. M. Jeon, M. H. Lee, G. H. Kim, X. Li, G. Park, B. Lee, S. Han, M. Kim, C. S. Hwang, *Nature Nanotechnology*. 456 (2010) 148.
- [38] S. A. Prosandeev, *J. Phys.: Condens. Matter* 14 (2002) L745.
- [39] L. Bengtsson, *Phys. Rev. B* 59 (1999) 12301.
- [40] J. Junquera, M. H. Cohen K. M. Rabe, *J. Phys.: Condens. Matter* 19 (2007) 213203.
- [41] L. Yu, V. Ranjan, M. B. Nardelli, J. Bernholc, *Phys. Rev. B* 80 (2009) 165432.
- [42] A. A. Demkov, A. Navrotsky, *Materials fundamentals of gate dielectrics*, Springer, Netherland, 2005, pp. 229.
- [43] A. K. Harman, S. Ninomiya, S. Adachi, *J. Appl. Phys.* 76 (1994) 8032.
- [44] X. Gonze, C. Lee, *Phys. Rev. B* 55 (1997) 10355.
- [45] M. Stengel N. A. Spaldin, *Nature* 443 (2006) 679.
- [46] B. Lee, C.-K. Lee, S. Han, J. Lee, C. S. Hwang, *J. Appl. Phys.* 103 (2008) 024106.
- [47] C.-K Lee, E. Cho, H. Lee, K. Seol, S. Han, *Phys. Rev. B* 76 (2007) 245110.

- [48] G. Mills, H. Jonsson, G. K. Schenter, *Surf. Sci.* 324 (1995) 305.
- [49] G. H. Vineyard, *J. Phys. Chem. Solids* 3 (1957) 121.
- [50] R. Krishnamurthy, Y. G. Yoon, D. J. Srolovitz, R. Car, *J. Am. Ceram. Soc.* 87 (2004) 1821.
- [51] S. Kirkpatrick, E. P. Stoll, *J. of Comp. Phys.* 40 (1981) 517.
- [52] U. Russo, D. Ielmini, C. Cagli, A. L. Lacaita, *IEEE, Electron Devices*, 56 (2009) 186.

CHAPTER 4

The nature of V_O in metal oxides

This chapter will involve the role of V_O in conductivity with respect to the defect energy level in band gap. We are going to discuss on the nature of V_O in In_2O_3 and SnO_2 . We carefully examine defect states induced by V_O within the band gap by employing GGA+U and hybrid functional to address the well-known experimental band gap. In addition, to avoid the finite cell-size effect, we carried carefully out the proper approaches to describe the isolated V_O in infinite cell. Based on the well-described the V_O in In_2O_3 and SnO_2 , it is found that the V_O has shallow and deep nature for In_2O_3 and SnO_2 , respectively.

4.1 The nature of V_O in In_2O_3

To ascertain the origin of intrinsic n-type conductivities of In_2O_3 , we investigate the nature of the V_O using the first-principles methods based on the GGA together with on-site correction, we find that main results such as the relaxation around the vacancy site significantly change with respect to the supercell size. It can be explained by the cross-behavior in the nature of V_O in In_2O_3 . In dilute limit, the V_O seems to be a shallow donor with the ionization energy of 0.15 eV. However, the transition level $\epsilon(2+/0)$ at 0.35 eV below the conduction band minimum cannot demonstrate the unintentional n-type conductivity of In_2O_3 at room temperature. In addition, when the vacancy defect is larger than 10^{20} cm^{-3} , we find that the character of the vacancy does not contribute to the electrical conductivity anymore. Furthermore, we investigate the vacancy-vacancy association, and find that the di-vacancy is stable with a binding energy of ~ 0.3 eV.

4.1.1 Introduction

The transparent conducting oxides (TCOs) such as ZnO , In_2O_3 and SnO_2 are technologically important materials that are widely used in various display and energy applications [1~3]. In_2O_3 have been attracting interests because of its excellent electrical

and optical properties [4]. In particular, Sn doped In_2O_3 (ITO) exhibit high carrier concentration up to 10^{21} cm^{-3} [5] is useful for electrode material in transparent TFT-LCD. [2] However, even though tremendous amounts of efforts have been devoted to understanding fundamental properties of In_2O_3 , there are still many issues that are not clearly understood. One of them is the conductivity of undoped In_2O_3 . It is well known that In_2O_3 grown in oxygen-poor conditions shows high intrinsic n-type conductivity with carrier densities up to 10^{20} cm^{-3} . [6–8] The carrier density and conductivity decrease with oxygen partial pressure, hinting that the defects related to oxygen deficiency may give rise to carrier generation.

Point defects such as metal interstitials [9,10] and oxygen vacancies (V_{O} 's) [4] are the first to be considered as both defects account for oxygen deficiency. Most calculations consistently support that V_{O} in In_2O_3 is more easily generated than metal interstitials. [9,11] However, the computational analysis disagrees on how deep the defect level is. While most calculations with generalized gradient approximation plus Hubbard U parameter (GGA+ U) or hybrid functionals show that V_{O} in In_2O_3 report both deep-level [9,11,12] and shallow-level characters [4, 13, 14]. In particular, P. Agoston et al. [13] and S. Lany et al. [15] are in controversy due to the uncertainty on defect energy level by V_{O} in band gap. They conclude that the band gap used to evaluate the donor ionization energy of V_{O} is important and that the accurate band gap is strongly required [16].

In this work, we try to resolve this issue in In_2O_3 by carrying out systematic first-principles calculations. First of all, one thing to which we paid particular attention is that the supercells (which consist of 80- and 160-atoms) employed in previous literature have the linear dimension of $\sim 1 \text{ nm}$. [17] Those supercells may not be enough if V_{O} in In_2O_3

has a shallow character with the large effective radius of the wavefunction, > 0.5 nm. Therefore, we increase the supercell containing one V_O site systematically to ensure that all computational results are about the single, isolated V_O . Based on those various supercell size, we investigate the electronic properties of V_O site and energy level of defect state by V_O from conduction band minimum (CBM) in order to ascertain the nature of V_O in In_2O_3 .

4.1.2 Calculation setup

Our first-principles calculations are based on density functional theory (DFT) using the projector-augmented-wave (PAW) potential as implemented in the Vienna Ab-initio Simulation Package (VASP) code. The cut-off energy for a plain-basis set is set to 500 eV. All atoms are allowed to relax until the force become less than 0.03 eV/Å. GGA and GGA+ U and hybrid method, HSE06 are used for the exchange-correlation potential. The well-known band gap underestimation in conventional-DFT makes estimation on defect state in band-gap difficult. In order to solve this issue, we have applied the GGA+ U and HSE06 method. For HSE06 (not shown here), although we could carry out just only about 80-atoms supercell due to its the high cost of calculation, the calculated electronic properties of V_O in In_2O_3 with 80-atoms are described similarly to GGA+ U results on same size.

Therefore, we can assume that GGA+ U is sufficient to describe the properties of V_O including gap-state even if band gap is still smaller than the value of experiment. In this

work, a value of $U = 7$ eV for the In- d states is used [18].

Table 4.1.1 enlists the supercells used in the present calculation. The supercells are constructed based on the conventional cubic cell except for 320-atoms cell which was obtained by multiplying the primitive cell (body-centered cubic). The nominal V_O density is also shown and it can be seen that the largest supercell correspond to the highest V_O density that might be obtained in experiment. In carrying out the first-principles calculations on TCOs such as In_2O_3 , special care is required for selecting k -points in Brillouin zone. This is because the conduction bands are highly dispersive and shallow defect levels may exhibit similar dispersions. For the 80-atom cell, $3 \times 3 \times 3$ k -points are found to ensure full convergence of defect formation energy (E^f ; see below) and atomic relaxations. The k points for larger supercells are scaled according to this reference density but the k point meshes are always shifted off the Γ point. This is because the wave function at the Γ point is much delocalized compared to other k points and the inclusion of the gamma point tend to result in too shallow levels and underestimation of E^f . This is the case even for the largest 1280-atoms supercell.

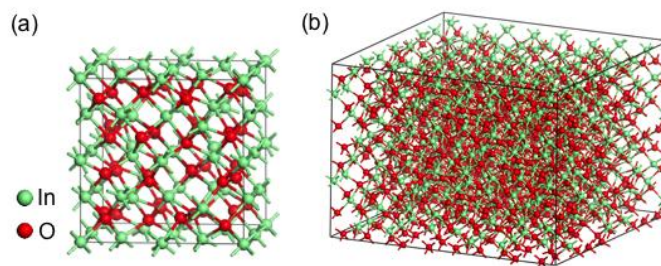


Figure 4.1.1 Model structure of In₂O₃. (a) A conventional cell and (b) the largest supercell in our study consisting of 80- and 1280-atoms, respectively.

Table 4.1.1. Cell dimension and V_O density corresponding to each supercell with various numbers of atoms. According to cell dimension, k-point meshes are selected in order to approach full convergence of V_O formation energy. k-point meshes are shifted off Γ - point.

Number of atoms	Cell dimension	V_O density ($\times 10^{20} \text{ cm}^{-3}$)	k-point mesh
80	$1 \times 1 \times 1$	10	$3 \times 3 \times 3$
160	$\sqrt{2} \times \sqrt{2} \times 1$	5.0	$2 \times 2 \times 3$
320	$2 \times 2 \times 2$ (primitive cell)	2.5	$2 \times 2 \times 2$
640	$2 \times 2 \times 2$	1.3	$2 \times 2 \times 2$
1280	$2\sqrt{2} \times 2\sqrt{2} \times 2$	0.6	(1/4,1/4,1/4)

4.1.3 Results and Discussion

4.1.3.1 Relaxation pattern of atoms around V_O site

We first examine the atomic relaxation around the vacancy site for the neutral and fully ionized state (V_O^0 and V_O^{2+} , respectively). In general, when V_O is a deep donor, the nearest cations tend to relax toward the V_O site (inward relaxation). This is because the defect levels are highly localized at the nearest metal atoms and the inward relaxation lowers the bonding energy by increasing the orbital overlap between metal atoms.

On the other hand, the ionic relaxation around V_O with shallow character is mainly dictated by the effectively positive charge of V_O which is only partially screened by the large defect states.

As such, cations and anions around this type of V_O relax outward and inward, respectively. A similar relaxation pattern should appear for V_O with resonant character.

In Fig. 1 (a), we display for each supercell the atomic displacement of nearest In and O atoms around V_O , in GGA and GGA+ U functional. It is found that In and O atoms always relax outward and inward, respectively (inset in Fig. 4.1.1 (b)). The most interesting feature in Fig. 4.1.1 (a) and (b) is that the displacement is significantly enhanced with the supercell size and in the largest supercell, the displacements are close to those for V_O^{2+} . Since the result in the largest supercell should be close to the diluted limit, it is strongly evidenced that the V_O in In_2O_3 is shallow or resonant and that the vacancy may behave like a deep donor if its density is close to $\sim 10^{21} \text{ cm}^{-3}$. The

pronounced suppression (mentioned above) in the first-shell relaxation in the large V_O defect density is closely related to the large dispersion of conduction bands in In_2O_3 . [19] The shallow or resonant character means that the two electrons produced by V_O lies in highly dispersive states. When the density of V_O is significantly high ($>10^{20} \text{ cm}^{-3}$), the energy of defect bands becomes significant. For example, at the highest V_O density of 80-atoms supercell, the Fermi level will be located at $\sim 1 \text{ eV}$ above the conduction minimum. Such a huge band energy can be effectively reduced by suppressing the first-shell relaxation as it lowers defect bands greatly.

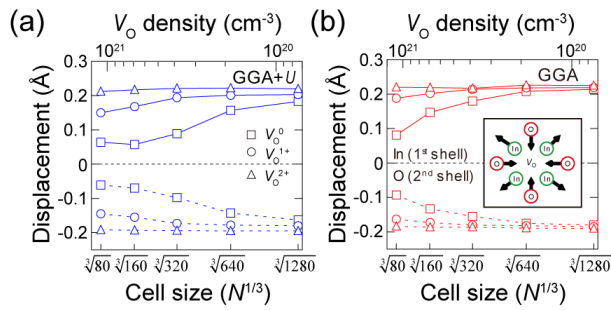


Figure 4.1.2 Displacement of relaxed atoms around V_O site in (a) GGA+ U (blue) and (b) GGA (red). Excepting V_O^{2+} , the other V_O state show that the displacement of atoms around V_O site is increased with cell size. Especially, for V_O^0 , the dependence is remarkably large, showing hindered relaxation at smaller cell.

4.1.3.2 Formation energy of charged V_O

We also estimated the formation energy of V_O in both functional in order to confirm the defect energy level of V_O in band gap from the formation enthalpy. The following formula was used for evaluating E^f :

$$E^f(V_O^q) = E_{tot}(V_O^q) - E_{tot}(\text{perfect}) + \mu_O + q(\text{VBM} + E_F) \quad (4.1)$$

where $E_{tot}(V_O^q)$ and $E_{tot}(\text{perfect})$ are total energies of supercell with and without a vacancy, respectively, and μ_O , the oxygen chemical potential and E^f is the position of the Fermi level with respect to the valence top (VBM). We set μ_O to the half of the O_2 energy and E^f is fix to VBM. In evaluating E^f of the charged vacancy, the correction scheme for Madelung energies were applied to account for spurious electrostatic interaction among periodic images. For ϵ_0 , we used the value calculated by using GGA+ U and GGA, 10.62 and 9.61, respectively.

In Fig. 4.1.2, we plotted E^f of V_O^0 , V_O^{1+} and V_O^{2+} as functions of L^{-1} and V^{-1} . For the finite-size corrections of the E^f of V_O , the cell size dependence was considered using GGA and GGA+ U . For charged V_O , E^f shows the L^{-1} and V^{-1} dependence and is almost constant with respect to cell size after subtracting the Madelung energies, applying the correction model by Makov and Payne [20]. From the right pannel of Fig. 4.1.2, E^f can be extrapolated to the dilute limit using V^{-1} dependence obtained by a linear fit.

It is notable that even for V_O^0 , E^f decreases with the cell size, particularly in GGA results, indicating the strong cell-size dependence. The difference of E^f of V_O^0 between at

the smallest, 80-atoms, and largest supercell, 1280-atoms, in our study is about 0.3 and 1 eV in GGA+ U and GGA, respectively. This result can be explained from the dispersive defect state with large effective radius to have to consider the overlapping between defects. Castleton et al [21]. reported that the dispersion of defect state can lead to errors in the formation energies of isolated defects at smaller cell size due to the connection between dispersive defect state. As cell size decrease, the elastic energy will be increase, giving rise to the higher formation energy. Because of the smaller displacement of first and second shell in GGA+ U than GGA, the elastic energy may be smaller, leading to the smaller variation of E^f of V_O^0 . Since the dispersion of defect level can lead to the uncertainty in the correct form for the scaling equation, we needed to consider the relaxation pattern of atoms around V_O site. As mentioned above. In dilute limit, V_O^0 and V_O^{2+} must show the similar effective charge of defect site, that is, doubly positively charged state, $+2e$. In case of high density of V_O , however, we can imagine that there is the screening of the effective charge by some electrons captured by suppressed relaxation around V_O^0 . If the screening effect is not considered, therefore, the linear cell-size dependence (L^{-1}) can be expected as like V_O^{2+} before subtracting Madelung energy, and we can obtain the E^f in infinite cell size using a linear fit as shown in the left panel in Fig. 4.1.2.

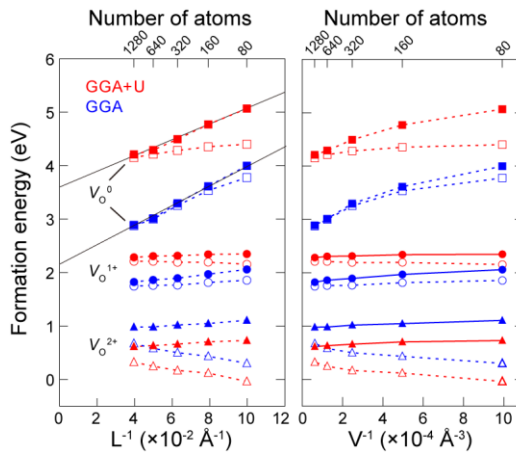


Figure 4.1.3 Formation energy of V_O in each charged state as a function of L^{-1} and V^{-1} . Open and closed symbols indicate the formation energy of each V_O before and after the correction. It is shown that GGA+ U and GGA show the same behavior in cell size dependence of formation energies. Solid lines are used for estimation of formation energy in dilute limit.

4.1.3.3 Defect charge transition level

In Fig. 4.1.3, we plotted the formation energies of V_O as a function of Fermi level in dilute limit within GGA+ U (blue) and GGA (red). V_O has a negative- U behavior, i.e., V_O^{2+} is almost stable charge state, V_O^0 is stable in a limited range near conduction band, and V_O^{1+} is unstable in a whole range of band gap. The transition level $\epsilon(2+/0)$ in both GGA+ U and GGA is found to be at about 0.35 eV below the conduction band minimum. In order to investigate the transition level when the band gap is extended to the experimental one, we also applied the GGA+ U approach with extrapolation [22] and plotted it (black line in Fig. 4.1.3). We found that the transition level is upshifted with the band gap and that the transition level at $E_C-0.35$ eV is fixed, indicating that the uncertainty of band gap is not a problem to determine the transition level of V_O .

4.1.3.4 Defect energy level in band gap

In order to clarify the defect character more clearly, we also examined the $\Gamma-\Gamma$ gap ($E_{\Gamma-\Gamma}$), the energy difference between valence band maximum and defect state at Γ -point. This is the distance of the V_O defect state from the valence band maximum (VBM) at the Γ -point. If the V_O is the resonant character, $E_{\Gamma-\Gamma}$ will converge to the bulk energy gap while the value will saturate at a value slightly lower than the bulk gap for the shallow vacancy. The results in Fig. 4.1.4 (a) show that both GGA+ U and GGA results well converge to the value of ~ 0.14 eV below the conduction band minimum. This

confirms that the V_O in In_2O_3 has the ionization energy of ~ 0.14 eV, good agreements with experimental donor ionization energy of 0.093 eV [23] and with the transition level $\epsilon(2+/0)$ of ~ 0.35 eV. It is surprising that $E_{\Gamma-\Gamma}$ agrees almost perfectly among GGA and GGA+ U calculations although the two functionals yields very different bulk energy gap (0.94 versus 1.83 eV). However, this can be understood from the shallow nature of the V_O . The Hubbard U parameter in GGA+ U calculations lowers the energy level of In- d states. Because of the shallow nature of the defect state, the wave function character is essentially identical between conduction bottom and the shallow defect level. Therefore, the influence of U parameter in shifting energy levels should be also similar between them, maintaining the energy difference between them. One may expect a similar behaviour in the hybrid functional calculations where the energy gap of 2.55 eV is correctly described.

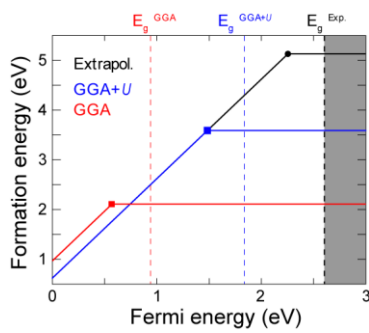


Figure 4.1.4 The transition level of V_O . It is described by using E^f in infinite cell-size estimated from Fig 4.2. The band gap of GGA and GGA+ U is 0.94 eV and 1.83 eV, respectively, smaller than the experimental value of 2.6 eV.

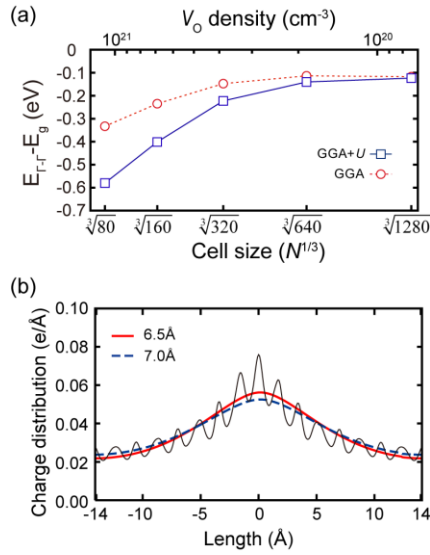


Figure 4.1.5 (a) Energy difference between CBM and V_O defect level at the Γ point as a function of V_O density. As cell size increase, the energy difference in both GGA and GGA+ U converge to ~ 0.1 eV that is close to the experimental donor ionization energy of 0.093 eV. (b) The y-z axis averaged charge distribution of V_O defect level at the Γ point in 1280-atoms supercell within GGA+ U . Red solid line and blue dashed line indicate the fitted $|\Psi(\vec{r})|^2$ with the effective radius of 6.5 Å and 7.0 Å, respectively.

4.1.3.5 The effective radius of defect state

In order to estimate the size of the shallow defect level, we plot in Fig. 4.1.4 (b) the partial charge density of the highest-occupied state at the Γ - point ($\Psi_{\Gamma}(\vec{r})$). This assumes that the state well represents the shallow defect level in the limit of the infinite supercell. Assuming that $\Psi_{\Gamma}(\vec{r})$ is a linear combination of the shallow defect level associated with each vacancy,

$$\Psi_{\Gamma}(\vec{r}) \sim \sum_{\vec{R}} e^{-|\vec{r}-\vec{R}|/a} \quad (4.2)$$

where \vec{R} is the lattice vectors of the supercell and a is effective radius of defect state. Fig. 4.1.4 (b) shows the averaged over y - z plane together with Eq. 4.2 with various a values. The a values of 5 to 10 Å are used. We estimate the root mean square (RMS) error between the partial charge density and Eq. 4.2 to find proper effective radius well-describing defect level. When $a = 6.5$ Å, RMS error was minimized. To evaluate the size of defect level, however, the tail part is more meaningful than other part. Therefore, without considering RMS error in the range of 5 Å from V_O position, we found that the fitted defect state has the effective radius of 7 Å. From the simple hydrogenic model, the size of the shallow level is given by the hydrogenic model ;

$$a_H^* = \frac{\hbar}{km^*(e^2/\epsilon_r)} = \frac{a_0\epsilon_r}{km^*/m_0} \sim 16.62 \text{ Å} \quad (4.3)$$

where k is coefficient constant of 1.69 to consider V_O^{2+} regarding as a helium atom

which consists of a nucleus of charge $+2e$. The calculated size is in good agreement with the fitted value of a , 7 \AA . Furthermore the calculated donor ionization energy is 0.14 eV . These makes sure of the delocalized nature of the vacancy defect.

4.1.3.6 The association of V_O 's

Lastly, we examine neutral V_O - V_O interaction in In_2O_3 using the largest 1280-atoms supercell. This is to investigate a possible defect clustering in In_2O_3 and its impact on the carrier density. We have considered various configurations for di- V_O in a given supercell and the lowest energy is always found when two V_O 's share two indium atoms (Fig.~\ref{fig:Binding} (c)). The interaction energy is calculated as follows:

$$E_{\text{int}} = E_{\text{tot}}(\text{near}) - E_{\text{tot}}(\text{far}) \quad (4.4)$$

where $E_{\text{tot}}(\text{near})$ indicates the total energy for the pairing of di- V_O and $E_{\text{tot}}(\text{far})$ means the total energy of when di- V_O are as far as possible from each other in a given supercell. In case of latter, its E is close to the one of a single V_O in half size of each given supercell. It indicates that di- V_O are sufficiently separated from each other.

The interaction energy between di- V_O is shown in Fig.4.5 (a). In case of GGA, the interaction energy is negative at higher defect density of $\sim 10^{21} \text{ cm}^{-3}$ indicating that di- V_O prefer pairing, giving rise to the localized state in band gap (the arrow in Fig. 4.1.5 (b)). As shown in Fig. 4.1.5 (c), two indium atoms sharing di- V_O are closer to each other by mediation of two electrons among four electrons generated from di- V_O , inducing the deep localized state [24] with lowered band energy. It indicates that the carrier concentration may be saturated at high V_O defect density, even if V_O in In_2O_3 induces

shallow or resonant state. At defect density of 10^{20} cm^{-3} , V_{O} 's tend to far from each other. It is a quite reasonable because of repulsive coulomb interaction of between V_{O} 's with positive charge. As defect density lower, the effect of defect density to V_{O} is reduced. Then the repulsive coulomb interaction becomes dominant, like in dilute limit. In contrast to GGA, for GGA+ U , we didn't find any positive interaction energy even if for the largest supercell of 1280-atoms. The V_{O} density may be still high.

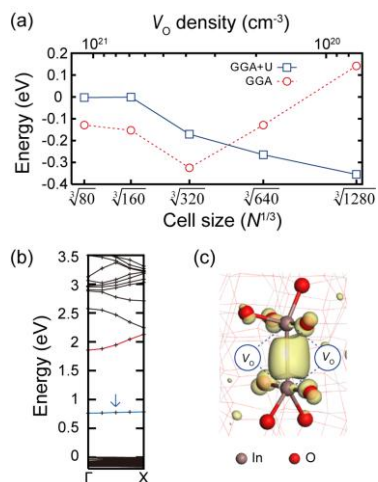


Figure 4.1.6 The association of V_O 's (a) The interaction energy of di- V_O 's as a function of V_O density. At high density ($> 10^{20} \text{ cm}^{-3}$), V_O prefer the pairing, holding two electrons (as shown in (c)). (b) Band structure and (c) partial charge density of the di- V_O .

4.1.3.7 The effect of pre-existing V_O 's

In order to investigate how the pre-existing V_O in the supercell affects the subsequent formation of V_O , we examine the difference in E^f and relaxation pattern between several cases. First, we made 640-atoms supercell with uniformly distributed 8- V_O as like 80-atoms supercell with single V_O , showing the same results about both the formation energy and relaxation pattern. Then, we made single V_O in 640-atoms supercell with the fully relaxed atomic-configuration of 7- V_O . The result showed that the atomic relaxation around V_O site formed newly is slightly uppressed. There are, however, no meaningful differences in E^f of V_O compared to E^f of single V_O in the supercell with uniformly distributed 8- V_O . These results indicate that the effect of pre-existing V_O 's is negligible with respect to forming new V_O 's in In_2O_3 , and that the nature of V_O is determined by whole V_O 's in In_2O_3 , including itself.

4.1.3.8 The effect of carrier density

We also considered that the V_O defect density can be regard as free electron carrier density with respect to giving rise to the influence on the properties of V_O , since two free electrons can be generated from V_O , shallow or resonant donor state in In_2O_3 . Using 1280-atoms supercell with single V_O , we added 2, 4 and 8 electrons to the supercell

which correspond to carrier densities of 640, 320 and 160-atoms supercell, respectively. We found that the relaxation of atoms around V_O site is suppressed when two electrons are added. In cases of both 4 and 8 electrons, however, there are no variations of degree of suppression even if electron carrier density increases. It seems that the effect of increasing carrier density is saturated quickly even if just small amount of electrons are increased. Also, the nature of V_O is critically affected by only V_O defect density.

4.1.4 Summary

we carried out systematic first-principle calculation in order to identify the nature of V_O in In_2O_3 . We found that in general, in dilute limit, V_O in In_2O_3 induces defect states at CBM-0.35 eV, regardless of the uncertainty of band gap of In_2O_3 , and that it has the ionization energy of ~ 0.15 eV. It indicates that V_O is hard to contribute to the n-type conductivity of In_2O_3 at room temperature, although it shows the delocalized character with the large effective radius. Moreover, at higher V_O defect density of $>10^{20} \text{ cm}^{-3}$, the defect state is deeper in order to lower band energy increased by high carrier density because of large dispersion of conduction band of In_2O_3 . In addition, at high V_O defect density, the di- V_O in In_2O_3 prefers the pairing, giving rise to deep localized defect state in band gap. Therefore, V_O cannot explain the n-type conductivity in In_2O_3 by itself, but should consider the extrinsic defects as like H_i . [25]

4.2 The nature of V_O in SnO_2

To ascertain the origin of intrinsic n-type conductivities of SnO , we investigate the nature of the V_O using the first-principles methods applying hybrid functional. For defective system, we carefully carried out the calculation on the formation energy of the V_O in dilute limit with the finite cell-size correction. We also describe the well-known experimental band gap using optimized HSE functional. We also estimate both thermal and optical ionization energy of the defect state by V_O and identify the deep nature of V_O , similar with the V_O in ZnO .

4.2.1 Introduction

Tin dioxide (SnO_2), known also as stannic oxids or cassiterite, is a key functional materials in many appications, such as transparent conducting electrodes, solar cells, and gas sensors. As a compound with a wide band gap ($E_g = 3.6 \text{ eV}$) [26] and high-dielectric constant (high-k), SnO_2 is also of general interest for the next generation gate oxides for Si-based electronic devices [27]. Owing to the fact that the oxide can relatively easily be doped, appropriate conduction band offset with Si may be achieved. Moreover, SnO_2 is also a potential candidate for applications in optoelectronics, such as in light emitting

diodes, laser diodes, etc. Indium tin oxide (ITO) is the current industrial standard material for transparent electrodes as thin films can be produced with resistivities of the order of $10^{-5} \Omega \text{ cm}$. However, due to the expense and rarity of indium, alternatives need to be found. Tin dioxide is a promising such material. The majority of TCO materials occur with n-type conductivity (SnO_2 , ZnO , In_2O_3). Although the conductivity is thought to be due to intrinsic defect formation, the exact mechanism is not well understood. Oxygen deficiency may be caused either by oxygen vacancies or tin interstitials, with reduction of some Sn(IV) ions to Sn(II) as a possible charge compensation mechanism as suggested by the observation of a SnO_2 phase in high-resolution transmission electron microscopy (HRTEM) [28] and fine structure emissions ascribed to Sn(II) in photoluminescence spectra [29]. Electronic conductivity could then occur due to the mobility of electrons from Sn(II) to Sn(IV) sites [30]. Experimental data suggests that the cause of the nonstoichiometry in SnO_2 is oxygen vacancies rather than tin interstitials. The measurement of conductivity as a function of O_2 partial pressure has shown results consistent with the V_{O} model [31]. There are few computational studies of defects in SnO_2 and these have concentrated mainly on energetics without analysis of the defect structure. Neither of these DFT studies presented detailed analysis of electronic structure, so the exact structure of intrinsic defects has yet to be determined.

4.2.2 Calculation setup

Our first-principles calculations are based on density functional theory (DFT) using

the PAW potential as implemented in the VASP code. The cut-off energy for a plain-basis set is set to 500 eV. All atoms are allowed to relax until the force become less than 0.03 eV/Å and 3x3x5 k-meshes are used for primitive cell consisting of two Sn atoms and two O atoms (Fig 4.2.1 (a)). The hybrid functional, HSE [26], are used for the exchange-correlation potential. To solve the well-known band gap underestimation in conventional-DFT, we used optimized mixing parameter of 0.32 (involving 32% Hartree-Fock exchange energy) to cancel out the self-interaction repulsive Coulomb energy. As mentioned above, the exact band gap is the most important for reliable estimation of defect states in band gap. For defect calculation, 128-atoms supercell shown in Fig 4.2.1 (b) is used for all calculation. For the spurious interaction between point defects in periodic supercell, the monopole-monopole correction by Makov and Payne is applied to the charged V_O calculation. Calculated structural parameters are listed in Table 4.2.1. SnO₂ crystallizes with the rutile structure, space group $P4_2/mmm(D_{4h}^{14})$, in which each Sn(IV) ion sits at the center of a slightly distorted oxygen octahedron (Fig. 4.2.1 (a)) [32]. Sn also possesses a lower +2 oxidation state, with Sn(II) adopting distorted 4-fold coordination in the corresponding monoxide SnO [33].⁶ In its stoichiometric form SnO₂ acts as an insulator, but in its oxygen-deficient form tin dioxide behaves as an n-type semiconductor with a band gap of 3.6 eV.

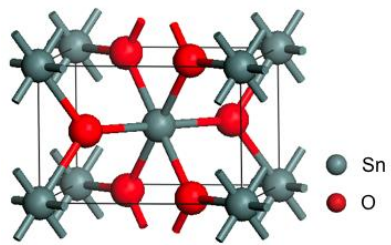


Figure 4.2.1 Model structure of SnO₂.

Table 4.2.1. Structural parameters of SnO₂.

	Our cal.	Exp.
a (Å)	4.742	4.73
c (Å)	3.181	3.18
E_g (eV)	3.6	3.6

4.2.3 Results and Discussion

4.2.3.1 Relaxation pattern of atoms around V_O site

We first examine the atomic relaxation around the vacancy site for the neutral and fully ionized state (V_O^0 and V_O^{2+} , respectively). Fig. 4.2.2 shows the relaxation pattern of the first-shell, Sn atoms, around the V_O site. There are two kinds of Sn atoms around the V_O site: one Sn bonded along in-plane directions and two Sn atoms bonded along out-of-plane direction. They show the similar relaxation pattern. For the second shell of O atoms, it is shown that their displacements are almost close to zero and that those can be negligible (not shown here). As shown in Fig. 4.2.2, V_O^0 and V_O^{2+} has the inward and outward relaxation pattern, respectively. For V_O^0 , although its displacement is small degree of 0.07 and 0.03 Å, 3% of the equilibrium Sn-O bonding length, Sn atoms are slightly moved toward the vacancy site, resulting in the localized defect state in band gap (Fig. 4.2.3). In Fig. 4.2.2 (b), the localized character of the neutral V_O can be identified in the partial charge distribution of defect state. Interestingly, this localized character of the neutral V_O in SnO_2 is contrast to In_2O_3 showing the shallow nature for the V_O^0 and to ZnO showing the first-shell atom's inward relaxation of 20% with respect to the bonding length for V_O^0 . For positively doubly charged V_O , V_O^{2+} , Sn atoms relaxed toward outward from the V_O site and its displacement is about 0.23 Å from the perfect lattice site. It results in the delocalized defect state and it is represented in Fig. 4.2.3. The defect states

occupied just small amount at the vacancy site and most states is spreaded out outward. It can be concluded that the V_O in SnO_2 shows the localized nature for neutral one, and that if it is charged emitting two electrons, the defect state is changed in character from deep to shallow or resonant. This tendency of realxation pattern of V_O is very close to that in ZnO showing the persistant photocurrent which induced by illumination. Therefore, for SnO_2 , PPC by the presence of V_O can be expected.

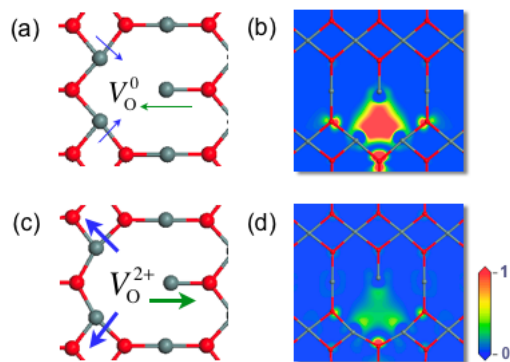


Figure 4.2.2 Relaxation pattern and partial charge distribution. (a), (b) V_O^0 and (c), (d) V_O^{2+} . Charge density is displayed by color mapping from blue to red corresponding to 0 to 1 electrons/V respectively.

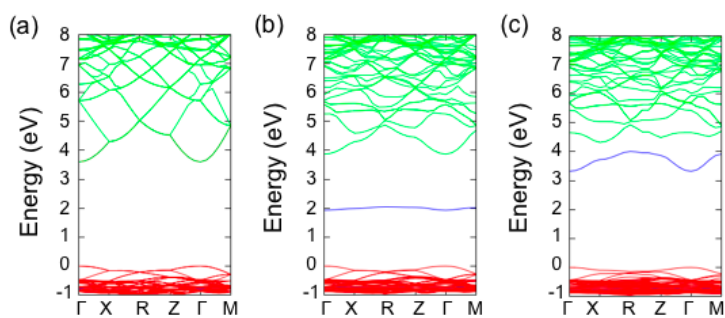


Figure 4.2.3 Band structure of (a) bulk, (b) V_O^0 and (c) V_O^{2+} . Defect state is represented by blue.

4.2.3.2 Band structures of SnO₂ containing V_O

In order to clarify the defect character more clearly, we also plotted the band structure of SnO₂ containing V_O. Fig. 4.2.4 displays the band structure for V_O⁰ and V_O²⁺ including perfect bulk SnO₂. For the bulk, it is shown the band gap of 3.6 eV in a good agreement with the experiments and that in contrast to the valence band, the conduction band is dispersive. However, when it contains the V_O, the conduction band undergoes the deformation hugely. Due to the deformation, more k-points mesh than the transition metal oxides are required to the defect properties of TCOs. As you can see in band structure of V_O, the defect state induced by V_O⁰ is located at ~ 2 eV above valence band maximum and at ~ 1.6 eV below conduction band minimum, indicating that the defect state of V_O⁰ may act as the trap site for electron carriers, which cannot contribute to the n-type conductivity of SnO₂. In contrast, for V_O²⁺, the defect state is upshift up into conduction band, resulting in the formation of the perturbed host state (PHS) mention by Junger. [36] It indicate that the defect state is populated in conduction band, i.e., the resonant state, generating two electrons as free carriers. These results also similar with ZnO. The V_O in SnO₂ seems to be similar with other TCO such as ZnO and Ga₂O₃ excepting In₂O₃ exhibiting the shallow nature of V_O even for the neutral case.

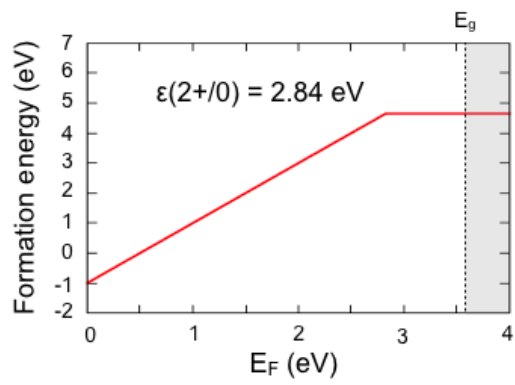


Figure 4.2.4 Formation enthalpy of V_O in SnO_2 . The experimental band gap of 3.6 eV is used to evaluate the thermal ionization energy of V_O .

4.2.3.3 Thermal ionization energy

We also estimated the formation energy of V_O in both functional in order to confirm the defect energy level of V_O in band gap from the formation enthalpy. Formation energies are calculated using the equation 3.1.1. In Fig. 4.2.4, we plotted the formation energies of V_O as a function of Fermi level in dilute limit within hybrid functional to describe the experimental band gap. V_O has a negative- U behavior, i.e., both V_O^0 and V_O^{2+} has the range of that they can be stable in band gap, however, V_O^{1+} is unstable in a whole range of band gap. This results in good agreements with previous reports. [34] The transition level $\epsilon(2+/0)$ is found to be at about 0.66 eV below the conduction band minimum. It represent that the thermodynamic ionization energy of V_O is about 0.66 eV and that V_O cannot be the source of the electron carrier in SnO_2 at room temperature.

4.2.3.4 Optical ionization energy

Upon photoexcitation, the electrons in the occupied DLS of V_O^0 are promoted into the conduction band, creating the ionized state V_O^{2+} . This process is described by the semiquantitative configuration coordinate diagram: first, both electrons occupy the deep and nonconducting state, V_O^0 . The average Sn-Sn distance, serving as the reaction coordinate, is small in this configuration ($d_{\text{Sn-Sn}} \sim 3.0 \text{ \AA}$). Optical excitation of the V_O^0

ground state to the $V_O^+ + e$ excited state occurs at the energy $e_0(1+/0) = +1.5$ eV. This transition creates V_O^+ having a singly occupied DLS within the band gap. The equilibrium Sn-Sn distance of V_O^+ is estimated as $d_{\text{Sn-Sn}} = 3.2$ Å. Due to the single occupancy of the DLS, the V_O^+ state is active in electron paramagnetic resonance (EPR), and is indeed observed in EPR experiments under illumination [34]. A second excitation $V_O^{1+} \rightarrow V_O^{2+} + e$ occurs at $e_0(2+/+) \sim +1.7$ eV, producing the V_O^{2+} state with $d_{\text{Sn-Sn}} = 4.0$ Å. Following this large outward relaxation, the DLS moves upward, becoming resonant inside the conduction band. Consequently, the photoexcited electrons occupy the lower energy PHS rather than the DLS, i.e., the V_O^{2+} vacancy assumes resonant behavior. The electrons in the PHS are now only shallowly bound through the screened Coulomb potential.

4.2.4 Summary

We carried out systematic first-principle calculation in order to identify the nature of V_O in SnO_2 . We found that in general, in dilute limit, V_O in SnO_2 induces defect states at CBM-1.6 eV under the experimental band gap of 3.6 eV, and that it has the thermal and optical ionization energy of 1.6 and 1.51 eV, respectively. It indicates that V_O in SnO_2 is hard to contribute to the intrinsic n -type conductivity of SnO_2 at room temperature, in contrast to In_2O_3 . Therefore, V_O cannot explain the n -type conductivity in SnO_2 by itself, but should consider the extrinsic defects [35] or the strain effect giving rise to the band edge engineering.

4.3 References

- [1] H. Hosono, *Thin Solid Films* 515, 6014 (2007).
- [2] K. Nomura, H. Ohta, A. Takagi, M. Hirano, and H. Hosono, *Nature* 432, 488 (2004).
- [3] K. Nomura, H. Ohta, K. Ueda, T. Kamiya, M. Hirano, and H. Hosono, *Science* 300, 1269 (2003).
- [4] P. Agostron, P. Erhart, A. Klein, and K. Albe, *J. Phys.: Condens. Matter* 21, 455801 (2009).
- [5] C. G. Granqvist, and A. Hultker, *Thin Solid Films* 411, 1 (2002).
- [6] H. Nakazawa, Y. Ito, E. Matsumoto, K. Adachi, N. Aoki, and W. Ochiai, *J. Appl. Phys.* 100, 0937061 (2006).
- [7] J. R. Bellingham, W. A. Phillips, and C. J. Adkins, *Thin Solid Films* 195, 23 (1991).
- [8] P. O. Bierwagen, and J. S. Speck, *Appl. Phys. Lett.* 97, 072103 (2010).
- [9] T. Tomita, K. Yamashita, Y. Hayafuji, and H. Adachi, *Appl. Phys. Lett.* 87, 051911 (2005).
- [10] P. D. C. King, R. L. Lichti, Y. G. Celebi, J. M. Cil, R. C. Vilao, H. V. Alberto, P. Duarte, D. J. Payne, R. G. Egdell, I. McKenzie, C. F. McConville, S. F. J. Cox, and T. D. Veal, *Phys. Rev. B* 80, 081201 (2009).
- [11] S. Lanuy and A. Zunger, *Phys. Rev. Lett.* 98, 045501 (2007).
- [12] A. Janotti, and C. G. Van de Walle, *Phys. Status Solid B* 248, 799 (2011).
- [13] P. Agoston, K. Albe, R. M. Nieminen, and M. J. Puska, *Phys. Rev. Lett.* 103, 245501 (2009).

- [14] P. Reunchan, X. Zhou, S. Limpijumngong, A. Janotti, and C. G. Van der Walle, *Current Appl. Phys.* 11, S296 (2011).
- [15] S. Lany and A. Zunger, *Phys. Rev. Lett.* 106, 069601 (2011).
- [16] P. Agoston, K. Albe, R. M. Nieminen, and M. J. Puska, *Phys. Rev. Lett.* 106, 069602 (2011).
- [17] P. P. Edwards, A. Porch, M. O. Jones, D. V. Morgan, and R. M. Perks, *Dalton Trans.* 2995 (2004).
- [18] P. Erhart, A. Klein, R. G. Egdell, and K. Albe, *Phys. Rev. B* 75, 153205 (2007).
- [19] Y. Kang, S. H. Jeon, Y.-W. Son, Y.-S. Lee, M. Rye, S. Lee, and S. Han, *Phys. Rev. Lett.*, 109, 12034 (2012).
- [20] G. Makov and M. C. Payne, *Phys. Rev. B* 51, 4014 (1995).
- [21] C. W. M. Castleton and S. Mirbt, *Phys. Rev. B* 70, 195202 (2004).
- [22] A. Janotti and C. G. Van de Walle, *Phys. Rev. B* 76, 165202 (2007).
- [23] R. L. Weiher, *J. Appl. Phys.* 33, 2834 (1962)
- [24] E. C. C. Souza, J. F. Q. Rey, and E. N. S. Muccillo, *Appl. Surf. Sci.* 255, 3779 (2009).
- [25] S. Limpijumngong, P. Reunchan, A. Janotti, and C. G. Van der Walle, *Phys. Rev. B* 80, 193202 (2009).
- [26] M. Batzill, U. Diebold, *Prog. Surf. Sci.* 79, 47 (2005)
- [27] J. Robertson, *Rep. Prog. Phys.* 69, 327 (2006); C. Kilic, A. Zunger, *Phys. Rev. Lett.* 88, 095501 (2006)
- [28] D. Maestre, J. Ramirez-Castellanos, P. Hidalgo, A. Cremades, J. M. Gonzalez-Calbet, J. Piqueras, *Eur. J. Inorg. Chem.* 1544 (2007)
- [29] F. Ming, T. Xiaoli, C. Xueli, Z. Lide, L. Peisheng, J. Zhi, *J. Phys. D: Appl. Phys.* 40,

7648 (2007)

[30] C. A. Vincent, *J. Electrochem. Soc.* 119, 515 (1972); B. Alterkop, N. Parkansky, S. Goldsmith, R. L. Boxman, *J. Phys. D* 36, 552 (2003)

[31] S. Samson, C. G. Fonstad, *J. Appl. Phys.* 44, 4618 (1973); J. Maier, W. J. Gopel, *Solid. State Chem.* 72, 293 (1988)

[32] T. Yamanaka, R. Kurashima, J. Z. Mimaki, *Kristallogr.* 215, 424 (2000)

[33] G. W. Watson, *J. Chem. Phys.* 114, 758 (2001).

[34] A. Janotti, and C. G. Van de Walle, *Phys. Stat. Sol. (b)* 1-6 (2010) ; P. Agoston, K.

Albe, R. M. Nieminen, and M. J. Puska, *Phys. Rev. Lett.* 103, 245501 (2009)

[35] S. Limpijumnong, P. Reunchan, A. Janotti, and C. G. Van de Walle, *Phy. Rev. B* 80, 193202 (2009)

[36] S. Lany, and A. Zunger, *Phys. Rev. B* 72, 035215 (2005)

CHAPTER 5

Conclusion

Semiconducting oxides have been attractive due to its potential to alter the silicon within the traditional devices. As usual, the oxygen deficient oxides exhibit better material properties than the stoichiometric oxides. Therefore, the V_O has been regarded as an important factor in material properties for the desired performance of devices consisted of oxides. However, the understanding on its role is not enough for controlling and engineering of the material properties of oxides because the experimental approaches have not been helpful due to its limitation in scale of observations. Therefore, in order to understand the role of V_O in atomic scale points of view, we employed the DFT calculation, a powerful tool to explore the quantum properties of materials.

First, for the understanding on the diffusion of the V_O , we carried out first-principles study on the electronic properties of GB in NiO, including point defects, V_O and V_{Ni} . It is

shown that the GB cannot be metallic even for non-stoichiometric GB, which means that it itself may be not the favorite path for electron carrier when the bias is applied. However, we founded that the ionic carrier such as a charged V_O can be moved along GB because of the lowered activation energy than bulk. As a result, we can conclude that the forming and rupture of filament current path in insulating poly-crystalline NiO can be explained by the migration of V_O along GB. Our results are in good agreements with experimental results. [1]

Then, in order to understand on how fast the V_O can be migrate in metal-oxide under field effect, we calculate the migration energy of V_O in various metal-oxides such as MgO, SrO₂ and Al₂O₃ applying the electric field. For this study, we have proposed a first-principles approach to simulate directly the charged V_O under the external field, and suggested the simple method to estimate a dielectric constant of oxides using “dielectric-constant meter”. From our results, we found that the lowered migration barriers by the field have not meaningful variation. Therefore, the external field itself cannot cause the fast redistribution of a charged single V_O . Nevertheless, the KMC simulations told us that the high-temperature condition is important for the fast redistribution of charged vacancies. It indicates that the electric field effect with respect to the migration of V_O can be explained by the heating of local temperature around V_O , leading to the increasing jumping-rat of V_O to another lattice site. Of course, the interaction between V_O 's such as forming of clustering can have other consequence, lowering the migration energy of V_O 's. However, our results are for the fundamental apprehension on the isolated V_O when the other effects are excluded, and it can help us to understand on the fast migration of single V_O in oxides.

Finally, to identify the nature of the V_O via the defect level and the association of V_O 's,

we carried out systematic first-principle calculation for In_2O_3 and SnO_2 . We found that V_{O} in In_2O_3 induces defect states at CBM-0.14 eV in dilute limit, regardless of the uncertainty of band gap of In_2O_3 , and that it has the ionization energy of 0.13~0.35 eV, which means that V_{O} in In_2O_3 has a shallow nature. For SnO_2 , the V_{O} induces defect states at CBM-1.6 eV under the experimental band gap of 3.6 eV, and that it has the thermal and optical ionization energy of 0.76 and 1.51 eV, respectively, indicating the deep character of V_{O} . These results tell us that V_{O} is hard to contribute to the n -type conductivity of both In_2O_3 and SnO_2 at room temperature, although the V_{O} in In_2O_3 shows the delocalized character. In addition, we also estimated on the association of V_{O} 's and found that at high V_{O} defect density, the di- V_{O} in In_2O_3 prefers the pairing, giving rise to deep localized defect state in band gap. As a result, we can conclude that the presence of V_{O} cannot explain the n -type conductivity in TCOs, even for In_2O_3 with the shallow nature of V_{O} . Therefore, for a further approach to the origin of n -type conductivity of TCOs, one need to consider another defects related to the oxygen atoms, such as a forming of peroxide, because its strong dependence on oxygen partial pressure of carrier concentration is hard to neglect. Of course, the extrinsic defect as like hydrogen interstitial, and its interaction with V_{O} can be one of possibilities for the origin. [2~4]

5.1 References

- [1] C. Park, S. H. Jeon, S. C. Chae, S. Han, B. H. Park, S. Seo, and D.-W. Kim, Appl. Phys. Lett. 93, 042102 (2008)
- [2] M.-H. Du, and K. Biswas, Phys. Rev. Lett. 106, 115502 (2011)
- [3] W. M. Hlaing Oo, S. Tabatabaei, M. D. McCluskey, J. B. Varley, A. Janotti, and C. G. Van de Walle, Phys. Rev. B 82, 193201 (2010)
- [4] C. G. Van de Walle, and A. Janotti, Mater. Sci. and Engin. 15, 012001 (2010)

산화물 반도체는 디바이스의 소재의 크기가 줄어들며 따라 누설전류와 같은 극복이 어려운 여러 한계점을 보이고 있는 실리콘의 대체 물질로서 많은 관심을 얻고 있다. 또한 산화물은 구성할 수 있는 구성 요소의 다양함으로 인해 기대할 수 있는 물성 또한 다양하기 하여 많은 분야에서 응용 되어질 수 있는 무한한 가능성도 지니고 있기 때문에, TFT와 디스플레이 패널과 같은 차세대 반도체 디바이스를 위한 가장 선호되는 물질이 되고 있다. 흥미롭게도, 산화물의 물성, 특히, 전기적 특성은 결정립계와 점결점과 같은 격자 불완전의 존재에 강하게 영향을 받는다. 특히, 산화물의 가장 기본적인 점결점인 산소결점은 산화물을 포함한 디바이스의 성능을 결정함에 있어 큰 역할을 하고 있다는 것이 잘 알려져 있다. 예로, 외부 전압에 의해 저항 변이 현상을 보이는 ReRAM의 작동원리는 전하를 띤 산소결점의 전자이동에 의한 산화물 내의 전도로의 형성 및 파괴에 의한 것으로 널리 받아들여지고 있다. 또한, 큰 밴드갭을 가지는 투명 전극 물질의 경우, 도핑이 되지 않은 물질에서도 *n*-type 전도성이 나타나며, 또한 증착시 산소 분압에 대한 전하 농도의 강한 의존성도 보여지고 있다. 이러한 사실들로부터 산소결점이 산화물의 물성과 관련하여 중요한 역할을 하고 있음을 알 수 있다.

이처럼, 산화물의 물성에 대한 산소결점의 중요성으로 인해, 산화물 내에서 산소결점의 역할에 대한 충분한 이해가 강하게 요구되어진다. 그러나 산소결점의 성질은 원자 단위에서 결정되어지기 때문에, 산소결점의 역할에 대한 연구 또한 원자 단위에서 이루어져야 한다. 그러나 해상도와 직접적인 측정의 어려움으로 인한 실험적 관측의 한계는 산소결점의 특성을

이해하기에는 역부족이다.

이 논문에서는, 산화물 내에서의 산소결점의 역할에 대해 이해를 얻기 위해 산소결점에 대한 3가지 관점, 즉, 산소결점의 확산과 결함준위, 산소결점간의 상호작용에 대해서 제일원리연구를 통한 원자 단위 수준에서의 분석을 수행하였다. 먼저 NiO와 같은 다결정 산화물 내에서의 산소결점의 이동에 관해 조사하였고, 결정립계와 같은 격자 불완전이 만들어내는 낮은 이동장벽으로 인해 산소결점이 쉽게 이동하는 경로가 될 수 있음을 확인하였다. 게다가, 여러 산화물 내에서 외부전압에 의한 산소결점의 전기적 이동에 대해서도 연구하였으며, 외부전압이 이동장벽을 낮추는 정도는 크기 않지만, 외부전압에 의한 Joule-heating 효과로 인해 산소결점의 이동이 더 빨리 일어날 수 있다는 것을 밝히었다.

두 번째로, 산소결점의 결점 특성과 관련하여, In_2O_3 와 SnO_2 와 같은 투명전극 물질 안에서의 산소결점이 산화물의 *n*-type 전도성에 대한 기여 여부를 알아보기 위한 연구를 수행하였다. 밴드갭 내의 산소결점의 결함준위 및 결점전하 전이 에너지에 대한 분석을 통해, 산소결점이 In_2O_3 내에서는 shallow 특성을, SnO_2 내에서는 반대로 deep 특성을 보여주는 것을 확인하였다. 그러나, shallow 특성을 보이는 In_2O_3 마저도 결점의 이온화 에너지가 상온에서 자유전하를 내놓을 만큼 작지 않음을 확인하였고, 이는 산소결점이 내재적인 *n*-type 정도성의 원인이 아닐 수 있음을 의미한다.

키워드: 제일원리연구, 산소결점, 반도체 산화물, 투명전극 산화물, ReRAM

학번: 2010-30785

전상호